# Manuscript Details

| | |
|---|---|
| **Manuscript number** | ATMOSRES_2019_1472_R2 |
| **Title** | Intensive Optical Parameters of Pollution Sources Identified by the Positive Matrix Factorization Technique |
| **Article type** | Research Paper |


**Abstract**

A new methodology based on optical parameters from integrating nephelometer measurements and chemically speciated PM10 mass concentrations, to associate intensive optical parameters with pollution sources identified by the Positive Matrix Factorization (PMF) technique, is presented. PM10 samplings and integrating nephelometer measurements at 450, 525, and 635 nm, co-located in space and time, were performed from November 2011 to November 2012. The PM10 samples were chemically characterized for 16 species, including ions (Na+, NH4+, K+, Mg2+, Ca2+, Cl-, NO3-, and SO42−), metals (Al, Cd, Cu, Fe, Mn, and Ti), OC, and EC. The scattering σs and backscattering βs coefficients at 450, 525, and 635 nm, and the PM10 chemically speciated data were used as input of the PMF model. Traffic (TRA, 28.3%), Biomass Burning and Nitrates (BBN, 27.4%), Soil Dust (SDU, 14.7%), ammonium Sulphate (SUL, 17.0%), and Aged Sea-salt (ASS, 12.6%) were the identified pollution sources, according to the PM10 mass apportionment, which did not show any significant difference in terms of source assignment and contribution, with respect to the solution without optical variables. The possibility of retrieving intensive optical parameters associated with the pollution sources from the related spectrally resolved σs and βs values is the main feature of the proposed approach. The mass scattering efficiency (□PM10), the scattering Ångstrom exponent (Å), the spectral curvature of the scattering Ångstrom exponent (□Å), and the asymmetry parameter (g) were the main intensive parameters calculated at different wavelengths or wavelength pairs to characterize the identified pollution sources. □PM10 and g at 450 nm, Å(450, 635 nm) and □Å were equal to 3.4 m-2 g, 0.57, 0.96, and 0.54 for the TRA-source, to 5.0 m-2 g, 0.58, 1.57, and -0.06 for the BBN-source, to 5.0 m-2 g, 0.67, 1.54, and 0.24 for the SUL-source, and to 0.6 m-2 g, 0.33, -0.65, and 0.12 for the ASS-source, respectively. The analysis of monitoring days with a prevailing pollution source and the comparison of the paper's results with literature values have demonstrated the reliability of the used methodology.



| | |
|---|---|
| **Keywords** | PM10 chemical composition; nephelometer measurements; intensive optical parameters; Positive Matrix Factorization; source apportionment |
| **Manuscript category** | Aerosol particles |



| | |
|---|---|
| **Corresponding Author** | Salvatore Romano |
| **Corresponding Author's Institution** | University of Salento |
| **Order of Authors** | Salvatore Romano, Roberta Vecchi, Maria Rita Perrone |


| | |
|---|---|
| **Suggested reviewers** | Christopher Cappa, Lucas Alados-Arboledas, Lauren Schmeisser, Olga Mayol-Bracero, Aurélien Chauvigné |

## Submission Files Included in this PDF

**File Name [File Type]**

second Response to Reviewer 1.docx [Response to Reviewers]

second Response to Reviewer 2.docx [Response to Reviewers]

HIGHLIGHTS - apportionment PMF Romano S et al.docx [Highlights]

second Revised Manuscript - paper PMF Romano S et ala.docx [Manuscript File]

declaration-of-competing-interests Romano S et al.docx [Conflict of Interest]

Credit Author Statement - Romano S et al.docx [Author Statement]

second marked copy - paper PMF Romano S et al.docx [e-Component]

REVISED supplementary material - Romano S et al.docx [Supplementary Material]

To view all the submission files, including those not included in the PDF, click on the manuscript title on your EVISE Homepage, then click 'Download zip file'.

## Research Data Related to this Submission

There are no linked research data sets for this submission. The following reason is given:
Data will be made available on request

## Highlights

"Intensive Optical Parameters of Pollution Sources Identified by the Positive Matrix Factorization Technique" by S. Romano, R. Vecchi, and M.R. Perrone

- A new methodology based on the PMF source apportionment was developed
- PMF was applied to nephelometer data and chemically speciated PM10 concentrations
- PMF identified traffic, biomass burning, soil dust, sulphate, and sea salt sources
- Sources were characterized by chemical profiles and intensive optical parameters
- Mass scattering efficiency differences among identified sources were highlighted

# Intensive Optical Parameters of Pollution Sources Identified by the Positive Matrix Factorization Technique

*S. Romano[1], R.Vecchi[2], and M.R. Perrone[1]*

[1]Dipartimento di Matematica e Fisica, Università del Salento, 73100, Lecce (Italy)

[2]Dipartimento di Fisica, Università di Milano, 20133, Milan (Italy)

**Abstract**

A new methodology based on optical parameters from integrating nephelometer measurements and chemically speciated PM10 mass concentrations, to associate intensive optical parameters with pollution sources identified by the Positive Matrix Factorization (PMF) technique, is presented. PM10 samplings and integrating nephelometer measurements at 450, 525, and 635 nm, co-located in space and time, were performed from November 2011 to November 2012. The PM10 samples were chemically characterized for 16 species, including ions ($Na^+$, $NH_4^+$, $K^+$, $Mg^{2+}$, $Ca^{2+}$, $Cl^-$, $NO_3^-$, and $SO_4^{2-}$), metals (Al, Cd, Cu, Fe, Mn, and Ti), OC, and EC. The scattering $\sigma_s$ and backscattering $\beta_s$ coefficients at 450, 525, and 635 nm, and the PM10 chemically speciated data were used as input of the PMF model. Traffic (TRA, 28.3%), Biomass Burning and Nitrates (BBN, 27.4%), Soil Dust (SDU, 14.7%), ammonium Sulphate (SUL, 17.0%), and Aged Sea-salt (ASS, 12.6%) were the identified pollution sources, according to the PM10 mass apportionment, which did not show any significant difference in terms of source assignment and contribution, with respect to the solution without optical variables. The possibility of retrieving intensive optical parameters associated with the pollution sources from the related spectrally resolved $\sigma_s$ and $\beta_s$ values is the main feature of the proposed approach. The mass scattering efficiency ($\Sigma_{PM10}$), the scattering Ångstrom exponent ($\mathring{A}$), the spectral curvature of the scattering Ångstrom exponent ($\Delta\mathring{A}$), and the asymmetry parameter ($g$) were the main intensive parameters calculated at different wavelengths or wavelength pairs to characterize the identified pollution sources. $\Sigma_{PM10}$ and $g$ at 450 nm, $\mathring{A}$(450, 635 nm) and $\Delta\mathring{A}$ were equal to 3.4 $m^{-2}$ g, 0.57, 0.96, and 0.54 for the TRA-source, to 5.0 $m^{-2}$ g, 0.58, 1.57, and -0.06 for the BBN-source, to 5.0 $m^{-2}$ g, 0.67, 1.54, and 0.24 for the SUL-source, and to 0.6 $m^{-2}$ g, 0.33, -0.65, and 0.12 for the ASS-source, respectively. The analysis of monitoring days with a prevailing pollution source and the comparison of the paper's results with literature values have demonstrated the reliability of the used methodology.

**Keywords**

PM10 chemical composition; nephelometer measurements; intensive optical parameters; Positive Matrix Factorization; source apportionment

## 1. Introduction

Atmospheric particles have different chemical, physical (size and shape), and optical properties being generated from different natural and anthropogenic pollution sources, and because of the changes they can undergo during the residence time in the atmosphere. Consequently, the atmospheric aerosol effects on human health, environment, and climate are characterized by high spatial and temporal variability, and continuous monitoring campaigns are required worldwide to properly estimate the impacts. Atmospheric aerosols influence the climate system directly by scattering and absorbing the solar and terrestrial (e.g., Yu et al., 2006) and indirectly by acting as cloud and ice condensation nuclei (e.g., Lohmann and Feichter, 2005). Considerable research activities have been developed to investigate the aerosol's role on climate (e.g., Hand and Malm, 2007) and the visibility degradation (e.g., Huang et al., 2010) by characterizing the aerosol optical properties, which in turn depend on the particle chemical composition and microphysical properties. Significant light-scattering properties are associated with organic particles, water-soluble inorganic species, such as sulphates or nitrates generally associated with fossil fuel/biomass combustion, and ammonium from fertilizers or biological sources (e.g., Charlson et al., 1992; Ten Brink et al., 1996; Haywood and Ramaswamy, 1998; Zhang et al., 2012). Carbonaceous particles as black carbon (BC) strongly absorbs light over a broad spectral range. In contrast, the colourless organic carbon (OC) has no or low absorption in the ultraviolet–visible (UV–VIS) spectral range (e.g., Costabile et al., 2017). Mineral dust and sea salt may significantly contribute to light scattering (e.g., Nousiainen and Kandler, 2015; Denjean et al., 2016; Fernández et al., 2017; Schmeisser et al., 2017; Pandolfi et al., 2018; Nicolás et al., 2019; Romano et al., 2019a) and mineral dust is a light-absorbing species (e.g., Rizzo et al., 2011; Ealo et al., 2016; Nicolás et al., 2018).

Nephelometers and aethalometers are widely used to monitor aerosol scattering and absorption coefficients, respectively, which represent the main extensive optical parameters characterizing aerosol populations. Based on these extensive parameters, different intensive aerosol optical properties can be calculated such as the Scattering and Absorption Ångström Exponents (SAEs and AAEs, respectively), which have commonly been used to identify different aerosol types and detect the main aerosol sources (e.g., Russell et al., 2014; Schmeisser et al., 2017). Romano et al. (2019a) used multi-wavelength nephelometer and aethalometer measurements to define a graphical framework, based on intensive optical parameters, and characterize different particles/particle mixture types at the study site. Perrone et al. (2014) used nephelometer measurements to investigate the impact of long-range transported air masses and meteorology on the aerosol optical properties at the surface. Then, Perrone et al. (2018) have shown that the Ångström exponent (SAE or Å, as it is

denoted in this work), retrieved from nephelometer measurements collocated in space and time with PM samplings, could represent a good parameter to better differentiate the chemical speciation of size-fractioned PM samples. It was shown that EC, $SO_4^{2-}$, and $NH_4^+$ reached the highest and the smallest mean mass percentage on the sampling days characterized by Å>1.2 and Å≤0.8, respectively. Conversely, primary and secondary organic carbon mean mass percentages reached the smallest and the highest value, respectively, on the days characterized by Å≤0.8.

Efforts have also been made over the past 50 years to extract source identification and apportionments from the chemical composition data of the ambient air, with the main goal of estimating the influence of pollution sources on air quality, as outlined in the review paper by Hopke (2016), and planning efficient remediation and mitigation strategies. The positive matrix factorization (PMF) technique has been successfully applied in numerous studies of ambient aerosols to determine main pollution sources (Hopke, 2016 and references therein). The PMF enables the apportionment of the measured chemical species mass concentrations and the quantitative evaluation of dominant sources (Paatero and Tapper, 1994). Perrone et al. (2013a) applied the PMF technique to chemically speciated PM1 and PM2.5 samples to identify main pollution sources at the monitoring site of this study. They found that most of the identified sources were characterized by similar chemical profile and seasonal trend in both the PM2.5 and the PM1 samples. Six pollution sources (combustion including biomass burning, ammonium sulphate, reacted dust, heavy oil combustion, secondary marine, and traffic) were identified by PMF in the PM2.5 samples. Perrone et al. (2019a) also applied the PMF technique to chemically speciated PM10 and PM2.5 samples, to retrieve main aerosol sources and contribute to the assessment of their impact on the PM weekly cycle both in Autumn-Winter and in Spring-Summer. Similar pollution sources were identified in PM2.5 and PM10 samples because of the significant contribution of fine mode particles at the study site, as mentioned in that paper.

Pauraite et al. (2018) applied the PMF to organic mass spectra retrieved from an aerosol chemical speciation monitor for PM1 particles with the main goal of assessing the influence of the chemical composition on the optical parameters of sources of organics. Forello et al. (2019) implemented a methodology based on both chemical and optical variables in a unique dataset that was analyzed by Multilinear Engine to retrieve the atmospheric absorption Ångström exponent of the sources and the mass absorption cross section (MAC) for fossil fuel emissions at different wavelengths. In previous studies, some of the authors have applied the PMF technique only to chemically-speciated data to characterize the chemical profiles of the identified pollution sources (Perrone et al., 2013a; 2019a).

In this study, PM10 samplings and multi-wavelength nephelometer measurements collocated in space and time have been performed at a coastal site of Southeastern Italy, with the main goal of identifying main pollution sources and characterizing them by both the optical and the chemical parameters. To

this end, the PMF technique was applied to the dataset obtained by integrating chemically-speciated data with corresponding optical parameters. The nephelometer measurements were only used in previous studies to characterize the optical parameters of the aerosol particles monitored at the receptor site (Perrone et al., 2014; 2015). As mentioned, a dataset made of chemical and optical parameters is used in this study to test the ability of the PMF technique. The ability of the proposed methodology to identify main PM10 pollution sources by PMF and characterize their chemical profiles and their optical properties by intensive and extensive optical parameters represents the main new aspect of this work.

## 2. Sampling site, instruments and methods

### *2.1. Site description and sampling instrumentation*

PM10 and PM1 samples were collected at ~10 m above the ground level at the Mathematics and Physics Department of the University of Salento, in a suburban area (40.4°N; 18.1°E) away from large pollution sources and considered representative of coastal sites of the Central Mediterranean (Perrone et al., 2013a; 2015). A (2.3 $m^3$ $h^{-1}$) HYDRA-FAI dual-sampler was used to simultaneously collect 24-hour PM10 and PM1 samples on 47-mm diameter quartz filters (PALLFLEX, Tissuquartz) pre-heated for 1 h at 700°C. Two daily PM10 and PM1 samples per week were on average collected from November 2011 to November 2012. The filters were conditioned for 48 h in an air-controlled chamber (25 °C and 50% humidity) before and after sampling and the PM mass was determined by gravimetric measurements. The uncertainties on mass concentration were lower than 5%. The PM10 loaded filters were divided in four portions for the determination of inorganic ions, metals, organic and elemental carbon.

### *2.2. Chemical analyses*

Soluble ionic species ($SO_4^{2-}$, $NO_3^-$, $NH_4^+$, $Cl^-$, $Na^+$, $K^+$, $Mg^{2+}$, and $Ca^{2+}$) were analyzed via High Performance Ion Chromatography (HPIC, Dionex DX-500 System). Samples were extracted in Milli-Q water: two successive extractions of 20 min (5 ml of water in each extraction) in an ultrasonic bath were used. The extracted solutions were analyzed by HPIC. Anion determination was performed by an Ion Pac® AS14A column (Dionex) using 1.8 mM $Na_2CO_3$/1.7 mM $NaHCO_3$ as the eluent at a 2 ml $min^{-1}$ flow rate and, for the detection, a conductivity system equipped with an ASRS®-ULTRA suppression mode (Dionex). Cation determination was performed by an Ion Pac® CS12A column (Dionex), using 20 mN $H_2SO_4$ as the eluent at a 1 ml $min^{-1}$ flow rate and, for the detection, a conductivity system equipped with a CSRS®-ULTRA suppression mode (Dionex). The method

detection limits (MDLs), expressed in μg $L^{-1}$, were 5.5 for $Cl^-$, 11 for $NO_3^-$, 8 for $SO_4^{2-}$, 11 for $C_2O_4^2$, 2 for $Na^+$, 3.5 for $NH_4^+$, 3 for $K^+$, 1 for $Mg^{2+}$, and 1.6 for $Ca^{2+}$.

For the metal analysis, acid digestion of the quartz filters was made with a MILESTONE MLS 1200 MEGA (FKV) microwave oven using 1 ml of $H_2O_2$, 2 ml of HF, and 4 ml of $HNO_3$. After cooling, 0.7 g of $H_3BO_3$ was added to aid the complexation of fluoride ions and to dissolve the formed fluoride salts. The final digestion was performed, and 20 ml of solution was obtained and analyzed. The samples were analyzed via Graphite Furnace Atomic Absorption Spectroscopy (GF-AAS, Pinnacle System) for determination of eight elements (Ni, Cu, V, Mn, As, Pb, Cr, and Sb) that were usually present in trace. Inductively Coupled Plasma Atomic Emission Spectroscopy (ICP-AES, Varian Liberty 110 spectrometer) was used for the analysis of four elements (Fe, Al, Zn, and Ti) present in major amount in collected samples. MDLs, expressed in μg $L^{-1}$, were 116 for Al, 2.6 for Zn, 8 for Fe, 3.6 for Ti, 0.6 for Sb, 0.15 for Cr, 0.08 for Cd, 0.6 for V, 0.06 for Cu, 1.5 for Ni, 1 for Mn, and 0.09 for Pb. Concentrations of the detected species were obtained with the removal of the average level present in the blank samples. The calculated concentration for a specific species was quantified if it was larger than the standard deviation $\sigma_B$ of the blank filters. Otherwise, a threshold value equal to $\sigma_B$ was considered. A concentration value equal to the maximum between the MDL and $\sigma_B$ was assumed if the concentration was below the MDL value or not detectable above the average variability of the field blanks.

The thermal optical transmittance technique by means of the Sunset Carbon Aerosol Analyzer (Birch and Cary, 1996) was performed with the NIOSH protocol (NIOSH, 1999) to determine elemental and organic carbon (EC and OC, respectively) in a 1.5-$cm^2$ filter punch (Perrone et al., 2009; 2011; 2013b). Uncertainties in the EC and OC measurements given by the manufacturer (Sunset Lab, OR) were estimated to be of the order of 5% ± 0.2 μg $cm^{-2}$.

*2.3 Nephelometer measurements*

Particle scattering ($\sigma_s$) and hemispheric backscattering ($\beta_s$) coefficients at 450, 525, and 635 nm were measured by a LED-based integrating nephelometer (model Aurora 3000, ECOTECH, Knoxfield, Australia) at a temporal resolution of 5 min. Müller et al. (2011) provided a description of the main features of the Aurora 3000 nephelometer. The air sampling was obtained from the top of a stainless steel tube, 15 mm internal diameter and about 1.5 m length. No aerosol size cut-off was applied to the sampled air and a relative humidity threshold of 60% was set by a processor controlled automatic heater inside the nephelometer (Perrone et al., 2018). The minimum scattering values measured at the study site were more than ten times larger than the corresponding detection limits as outlined in

Perrone et al. (2018). Some results on the particle scattering properties from nephelometer measurements for the monitoring site of this study have been reported in Perrone et al. (2014, 2015).

*2.4. Receptor modelling*

The Positive Matrix Factorization technique is a well-known modelling approach (PMF, EPA-PMF v.5.0, Norris et al. (2014)) that can be expressed as X = GF+E, where X is the known n by m matrix of the m measured species in n samples. G is an n by p matrix of source contributions to the samples (time variations of factors scores). F is a p by m matrix of source profiles and E is defined as a residual matrix, i.e. the difference between measurement and model outputs.

In this paper, PMF was applied to the dataset (X) including PM10 chemically speciated data (Al, Cr, Cu, Fe, Mn, Ti, $Cl^-$, $NO_3^-$, $SO_4^{2-}$, $Na^+$, $NH_4^+$, $K^+$, $Mg^{2+}$, $Ca^{2+}$, OC, and EC) and the aerosol scattering and backscattering coefficients at 450, 525, and 635 nm to retrieve the main emission sources affecting the study area. Forello et al. (2019) showed that the PMF analysis can be performed on joint datasets. Indeed, if different units are present in different columns of matrix X, the output data in factor matrix G are pure numbers and elements in a column of factor matrix F carry the same dimension and unit as the original data in matrix X. Of course, the average total contribution to the mass of a specific source due to species in a certain factor in matrix F must be retrieved a-posteriori, summing up only mass contributions by chemical components (i.e. excluding optical components in matrix F).

All the selected variables were classified as strong according to the signal-to-noise criterion reported in Paatero (2015). The dataset consisted of 82 entries/samples and 23 variables including the PM10 mass concentration as an independent variable to provide direct mass apportionment, down-weighing the mass by a factor 4 (Kim and Hopke, 2007; Vecchi et al., 2008). A 15% uncertainty was associated to elements and EC, 10% to ions and OC, and 20% to optical variables. The procedure suggested by Polissar et al. (1998) was adopted to treat uncertainties as well as missing data.

## 3. Results and discussion

*3.1. PM10 concentration and chemical characterization*

The dataset of this study is based on 82 PM10 samples. Table 1 shows the yearly mean values of PM10 and corresponding chemical species mass concentrations ± Standard Error of the Mean (SEM), in addition to Autumn-Winter (AW, October-March) and Spring-Summer (SS, April-September) mean values ±SEMs. The mean mass percentages of the measured species with respect to the total sampled mass are reported in brackets. The PM1/PM10 mass ratio is also given in Table 1 to highlight

the seasonal impact of the fine mode particle contribution on PM10. Note that the simultaneous PM10 and PM1 samplings has allowed in Perrone et al. (2016) to identify the Saharan dust impact on the chemical composition of PM10 and PM1 samples.

Table 1 shows that the mean PM10 mass concentration and PM1/PM10 mass ratio decrease slightly from AW to SS. The mass percentage of $Na^+$, $NH_4^+$, $Mg^{2+}$, $Ca^{2+}$, and $SO_4^{2-}$, and of all tested metals is greater in SS than in AW. The mass percentage of $K^+$, EC, and OC is weakly dependent on seasons. Conversely, the mass percentage of $NO_3^-$ is greater in AW than in SS. Previous analyses showed that the ground level PM properties are season dependent at the study site (e.g., Perrone et al., 2009, 2011, 2013b, 2015; Pietrogrande et al., 2018). A detailed discussion on the PM10 chemical speciation and seasonal dependence is provided in Perrone et al. (2018; 2019a; 2019b). Note that the dataset of this study is a subset of the one reported in Perrone et al. (2016; 2018).

### *3.2 Characterization of optical properties from experimental measurements*

Yearly, AW, and SS mean values (± SEM) of the scattering and backscattering coefficients at 450, 525, and 635 nm, retrieved from nephelometer measurements collocated in space and time with the PM10 samplings, are given in Table 2. The scattering and backscattering percentage differences $\Delta\sigma_s$ and $\Delta\beta_s$, respectively, calculated from the corresponding $\sigma_s$ and $\beta_s$ values at 450 and 635 nm, are also shown. The main statistical parameters of the scattering Ångström exponent ($\mathring{A}$) and the scattering Ångström exponent difference ($\Delta\mathring{A}$) calculated from $\sigma_s$ values (Schuster et al., 2006) are also in Table 2. $\mathring{A}$ is calculated at the 450–635 nm wavelength pair by the following relationship:

$$\mathring{A}\ (450\ \text{nm}, 635\ \text{nm}) = -\ln\left[(\sigma_s\ (450\ \text{nm})/(\sigma_s\ (635\ \text{nm})\right]/[\ln\ (450/635)] \quad (1)$$

and $\Delta\mathring{A}$ by the following relationship:

$$\Delta\mathring{A} = \mathring{A}\ (450\ \text{nm}, 525\ \text{nm}) - \mathring{A}\ (525\ \text{nm}, 635\ \text{nm}) \quad (2)$$

$\sigma_s$ and $\beta_s$ are extensive parameters since they depend on the particle number concentration and type. Conversely, $\mathring{A}$ and $\Delta\mathring{A}$ are intensive optical parameters, since they only depend on the particle type. The scattering Ångström exponent represents the wavelength dependence of the scattering coefficient and it is related to the mean size and relative concentrations of the accumulation and coarse-mode aerosols (Wang et al., 2015): the smaller is the particle size the larger is the $\mathring{A}$ value. In general $\mathring{A}<1$ refers to coarse mode particles and $\mathring{A}>1$ represents populations dominated by fine mode particles. Schuster et al. (2006) have shown that $\mathring{A}$ alone does not provide unambiguous information on the relative weight of coarse and fine mode particles, if particles are characterized by a bimodal/multimodal size distribution, as at the monitoring site of this study (e.g., Perrone et al., 2018).

In fact, large fine mode particles can have the same $\AA$ as mixtures of coarse and small fine mode particles. Then, some authors (e.g., Kaufman, 1993; O'Neill et al., 2003; Schuster et al., 2006) have demonstrated that $\Delta\AA$ can provide information on the contribution of fine and coarse mode particles. Negative $\Delta\AA$ values indicate a dominance of a single small particle mode, while positive values indicate the effect of two separate particle modes, according to Schuster et al. (2006). Consequently, $\Delta\AA$ increases with the contribution of the coarse mode particles as shown by Perrone et al. (2014) and Perrone and Burlizzi (2015).

Table 2 shows that the scattering and backscattering coefficient mean values decrease from AW to SS (significant at the 95% confidence level based on a two-tailed t-test), in accordance with the PM10 mass concentration to which are strongly linked (Andreae et al., 2002; Perrone et al., 2014). The $\sigma_s$ and $\beta_s$ decreased with the increase of the wavelength (significantly at the 95% confidence level based on a two-tailed t-test), as the $\Delta\sigma_s$ and $\Delta\beta_s$ percentage changes show (Table 2). This result is likely due to the significant role of fine mode particles at the study site, as proved by the $\AA$ mean value (>1). Table 1 also shows that 41% and 38% of the PM10 mass is due to PM1 particles in AW and SS, respectively (Table 2), with a seasonal variation statistically significant at 90% confidence level. Consequently, $\AA$ assumes a slightly higher mean value in AW than in SS. Therefore, $\sigma_s$, $\beta_s$, $\Delta\sigma_s$, $\Delta\beta_s$, and $\AA$ mean values indicate that fine particles are likely prevailing at the study site and that their contribution decreases from AW to SS. The $\Delta\AA$ mean value, which is positive and increases from AW to SS, shows the effect of two separate particle modes and suggests that the coarse particle contribution increases from AW to SS. The SS increase of the mass concentration of $Na^+$, $Mg^{2+}$, $Ca^{2+}$, Al, Cr, Fe, Mn, and Ti, which are on average associated with coarse particles (e.g., sea-salt, resuspended dust; Seinfeld, 1986), supports the above findings.

The asymmetry parameter $g$ is also calculated, since it is one of the main parameters required in radiative transfer simulations. It provides a measure of the angular distribution of the scattering radiation (e.g., Seinfeld and Pandis, 1998; Tafuro et al., 2007) being equal to zero for symmetric (e.g., Rayleigh) light scattering and to one for entirely forward scattering (e.g., Bergamo et al., 2008). Wiscombe and Grams (1976) found the following relationship between the $\beta_s/\sigma_s$ and $g$ from Mie calculations (Andrews et al., 2006):

$$g = -7.143889 \cdot (\beta_s/\sigma_s)^3 + 7.464439 \cdot (\beta_s/\sigma_s)^2 - 3.96356 \cdot (\beta_s/\sigma_s) + 0.9893 \quad (3)$$

which indicates that $g$ decreases regularly with the $\beta_s/\sigma_s$ ratio. The $g$ mean values decreased with the increase of the monitoring wavelength and did not show any significant seasonal dependence within ± SEM (Table 2). In a more detail, the temporal evolution of $g$ (with a yearly mean value at 450 nm equal to 0.59±0.01) during the analyzed period was reported and discussed in Perrone et al. (2015).

Note that $g$ is generally higher for larger particles (e.g., marine and/or dust aerosol) compared to fine particles (e.g., anthropic/urban aerosol) in most of the shortwave region (e.g., Mallet et al., 2003). The variability of $g$ as a function of different mean particle sizes will be described in the following by some case studies (Section 3.5).

The mass scattering efficiency ($\Sigma_{PM10}$) of the sampled PM10 particles is calculated from the slope of the best line fitting the $\sigma_s$ versus the corresponding PM10 mass concentration. Both $\sigma_s$ and PM10 mass concentrations depend on number concentration of the atmospheric particles, and $\sigma_s$ could also be used to estimate PM mass concentration. Therefore, the mass scattering efficiency is a complex function of particle size, shape, composition, hygroscopicity, and mixing state (Andreae et al., 2002; Hand and Malm, 2007, Latimer et al., 2019). Table 2 shows the yearly, AW, and SS $\Sigma_{PM10}$ means calculated at 450, 525, and 635 nm from the daily mean PM10 mass concentrations and the corresponding scattering coefficients at different wavelengths. The $\Sigma_{PM10}$ spectral dependence reflects the $\lambda^{-\mathring{A}}$ dependence of $\sigma_s$ (Kokhanovsky, 2008), where $\lambda$ is the wavelength. One also observes that the $\Sigma_{PM10}$ mean value decreased more than 50% from AW to SS at all wavelengths. A similar seasonal trend was also observed by Titos et al. (2012) analyzing PM10 samples in another Mediterranean site (Granada, Southern Spain). They explained that the $\Sigma_{PM10}$ seasonal pattern is closely related to main differences in PM composition. In particular, the mineral dust, whose contribution generally increases during the warm seasons (as also proved by the $\mathring{A}$ decrease and the $\Delta\mathring{A}$ increase in SS), is less efficient in term of scattering radiation with respect to the aerosol particles that predominate in winter. Perrone et al. (2018) reported a sensitivity study of $\Sigma_{PM10}$ as a function of different $\mathring{A}$ ranges at the same site of this work, proving the decreasing trend of $\Sigma_{PM10}$ by increasing the mean particle size.

### *3.3 PMF source apportionment by accounting chemical and optical properties*

Different solutions (from 4 to 7 factors) have been explored and finally the most physically robust one was the 5-factor solution. Indeed, a larger number of factors produced not acceptable solutions characterized by null mass and being difficult to be associated with meaningful sources. The selected solution had $R^2$=0.70 and the PM10 mass was reconstructed within 16% (slope = 0.84 and negligible intercept), also the input variables were well reconstructed (generally $R^2$>0.8 with only a few exceptions with $R^2$>0.5). Scaled residuals were generally within ± 3 standard deviations and followed a Gaussian distribution; only in 10% of the cases, the residual was out of the above-defined interval, but typically within four standard deviations.

The factor-to-source assignment was tentatively done by considering both the percentage of the chemical species in the factor and the factor chemical profiles (see Fig. SM1 of the Supplementary

Material (SM) file) identifying the following sources: Traffic (TRA), Biomass Burning + Nitrates (BBN), Soil Dust (SDU), ammonium Sulphate (SUL), and Aged Sea-salt (ASS). Factor fingerprints are shown in Fig. SM2. Typical source tracers (see e.g. Viana et al., 2008; and references therein) were identified for traffic (e.g., Cu, Fe, EC, and OC), biomass burning and nitrates (e.g., $K^+$, EC, OC, and $NO_3^-$), soil dust (e.g., Al, Ti, Fe, and Mn), ammonium sulphate (i.e., $SO_4^{2-}$ and $NH_4^+$), and aged sea salt (e.g., $Na^+$, $Cl^-$, and $Mg^{2+}$) from the species percentages. The latter source was ascribed to aged marine air masses, since the typical diagnostic ratio Cl-to-Na was less than 1 (instead of 1.8 typical for bulk sea water). This last result may be associated with the well-known Cl depletion process to which advected marine air masses undergo when interacting with polluted air masses (see e.g. Seinfeld and Pandis, 1998). The diagnostic ratio of other sea salt components like e.g. the Mg-to-Na was not affected by this process since it resulted to be 0.18 (vs. 0.12 in bulk sea water) in this profile. The PMF analysis was also performed using only the chemical dataset: the results in terms of source assignment and contributions did not show any significant difference with respect to the solution including the optical variables here presented.

*3.3.1 PM10 mass source apportionment*

Figure 1a shows the apportionment of the PM10 mass considering the whole dataset (from November 2011 to November 2012): traffic (28%), biomass burning+nitrate (27%), soil dust (15%), ammonium sulphate (17%), and aged sea-salt (13%). Mean ± SEM values of the PM10 mass concentration associated with the PMF pollution sources are in Table 3. Most of the sources here identified are similar to the ones detected and investigated in previous studies referring to different study periods at the same site of this work (e.g., Perrone et al., 2013a; 2019a). Averages of the source contributions for AW (March-October data) and SS (April-September data) are reported in Figure 1b and 1c, respectively.

The contribution of the biomass burning+nitrate (BBN) source, which is the dominant pollution source in AW (44%), decreases to 13% in SS. It is characterized by high contributions due to OC, EC, $NO_3^-$, and $K^+$ (Figs. SM1 and SM2), which are the dominant chemical components of PM10 in addition to $SO_4^{2-}$, $NH_4^+$, and $Ca^{2+}$ (Table 1). The BBN source decrease from AW to SS (> 70%) was associated with a decrease of the OC, EC, $NO_3^-$, and $K^+$ mass percentages (Table 1), also because of the residential heating contribution decrease. Note that nitrate generally reaches its maximum concentration in AW in the form of $NH_4NO_3$ and, then, decreases in SS due to its decomposition related to the enhanced temperatures occurring during the warm seasons (e.g., Yubero et al., 2015).

The contribution of the Traffic (TRA) source, which is the dominant pollution source in SS (35%; Fig. 1c), is 20% in AW (Fig. 1b). It is characterized by high contributions due to $Ca^{2+}$, Cr, Cu, Fe,

Mn, OC, and EC (e.g., Minguillòn et al., 2012). The TRA source increase from AW to SS (~ 75%) was associated with the increase of the corresponding tracers: $Ca^{2+}$, Cr, Fe, and Mn mass percentages experienced a significant increase from AW to SS, as reported in Table 1.

The Soil Dust (SDU) source is the second most abundant source in SS (22%; Fig. 1c). Its decrease to 6% in AW (Figure 1) was associated with a corresponding decrease of the related marker species: Al, Fe, Mn, Ti, and $Ca^{2+}$ percentage contributions significantly decreased from SS to AW (Table 1). The typical meteorological conditions occurring in SS all over the Mediterranean basin, which favored the air mass aging, enhanced soil dust resuspension and limited its removal by wet deposition (e.g., Querol et al., 2009; Perrone et al., 2015) contributed to the above results and, therefore, to the seasonal changes of the SDU source contribution.

The ammonium sulphate (SUL) source contributes almost equally in AW and SS (Figs. 1b and 1c, respectively). This last result was mainly due to the high mass percentage contribution of the SUL source in February and March of the monitoring year (2012) with respect to the corresponding April and May percentage contributions, as the monthly analysis of mass percentages showed. Note that a weak seasonal dependence of the Aged Sea-salt (ASS) source was on average observed at the study site (e.g., Perrone et al., 2019a). Accordingly, Table 1 shows that $Na^{+}$, $Cl^{-}$, and $Mg^{2+}$, which are the main tracers of the ASS source (Figs. SM1 and SM2), did not present any significant seasonal variation. These last results could be related to the geographical location of the study site, at the center of a narrow (~ 40 km) peninsular area, thus affected by the sea-salt advection from two different seas (Ionian Sea and Adriatic Sea).

*3.3.2 Scattering and backscattering coefficient apportionment to pollution sources*

Table 3 shows mean values (±SEM) of the scattering and backscattering coefficients at 450, 525, and 635 nm associated with the PMF identified pollution sources, in addition to the scattering and backscattering percentage differences calculated for each pollution source. The greatest $\sigma_s$ and $\beta_s$ mean values are associated with the BBN pollution source at all wavelengths. The PM10 mass concentration associated with the BBN source also assumes one of the highest values (Table 3). In contrast, a null $\sigma_s$ value and the smallest $\beta_s$ value are associated with the SDU source at 450, 525, and 635 nm (Table 3). It is also noteworthy that the PM10 mass concentration associated with the SDU source assumes one of the smallest values. Rather small $\sigma_s$ and $\beta_s$ mean values are also associated with the ASS pollution source at all wavelengths. The rather weak sensitivity of the scattering and backscattering coefficients to the prevailing particles of the SDU and ASS sources has likely contributed to these last results. Figure 2 shows the seasonal dependence of the spectrally resolved $\sigma_s$ contributions to pollution sources, in addition to the corresponding $\Delta\sigma_s$ values. The scattering of small

particles is more pronounced at shorter wavelengths and the scattering of large particles is more pronounced at longer wavelengths, according to Lopatin et al. (2013). Consequently, the rather high $\Delta\sigma_s$ value that characterizes the BBN and SUL sources is likely due to the significant contribution of fine mode particles to both sources, as it is commonly assumed (Seinfeld and Pandis, 1998). In contrast, the ASS-$\Delta\sigma_s$ value is negative (-25%) since the ASS-$\sigma_s$ is slightly more pronounced at long wavelengths (Table 3), because of the significant contribution of coarse mode particles (Seinfeld and Pandis, 1998). The ASS- and SDU-$\beta_s$ mean values also increase with the wavelength. More specifically, the $\Delta\beta_s$ values associated with the ASS and SDU source that are equal to -23 and -61%, respectively, likely suggest that the contribution of coarse particles to the SDU source is far greater than that of the ASS source. Consequently, a null $\sigma_s$ value is associated by the PMF with the SDU source. The prevailing contribution of coarse particles to soil dust sources has been outlined in previous studies (e.g., Seinfeld and Pandis, 1998).

Figure 3a shows the source apportionment of scattering coefficient at 450 nm for the whole dataset: traffic (30%), biomass burning+nitrate (42%), soil dust (0%), ammonium sulphate (26%), and aged sea-salt (2%). The $\sigma_s$(450 nm) source apportionment for AW and SS is shown in Fig. 3b and 3c, respectively. The seasonal dependence of $\sigma_s$(450 nm) and the corresponding percentages apportioned to the identified pollution sources for AW (Figs. 2b and 3b) and SS (Figs. 2c and 3c) are similar to the ones of the PM10 apportionment (Fig.1). The BBN source is the prevailing one in AW. The TRA and SUL sources are the prevailing ones in SS, while the ASS source is weakly dependent on seasons.

*3.4 Intensive optical parameters of the identified pollution sources*

A discussion on the intensive optical parameters ($\AA$, $\Delta\AA$, $\Sigma_{PM10}$, and $g$) associated with the PMF-pollution sources is presented in this subsection. Paper's results are compared in Table 4 with literature values to support their reliability. The intensive optical parameters associated with a specific pollution source are season independent, as expected. In contrast, the extensive parameters (PM10, $\sigma_s$, and $\beta_s$) associated with a pollution source may be season dependent, as outlined in the previous sections.

Table 3 shows that the BBN source is characterized by the highest (1.57) and the smallest (-0.06) $\AA$ and $\Delta\AA$ values, respectively. Negative $\Delta\AA$ values indicate a dominance of a single small particle mode, as mentioned in Schuster et al. (2006), and the BBN-$\Delta\sigma_s$ value, which reaches the highest value (Table 3), supports last comment. Clarke and Kapustin (2010) used the value of $\AA$ (450, 550 nm) = 1.3 as a dividing line between air masses affected by smaller particles from combustion sources ($\AA$ (450, 550 nm) >1.3) and by coarse-mode particles, such as sea salt and mineral dust ($\AA$ (450, 550 nm)

<1.3). This last result is in good accordance with the findings by Cappa et al. (2016) and Costabile et al. (2013), both from surface in situ measurements (Table 4). In fact, Cappa et al. (2016) found that the biomass burning aerosol was characterized by *Å* (450, 550 nm) >1.5, while Costabile et al. (2013) characterized the small accumulation mode particles rich in black carbon from biomass smoke by diameters spanning the 120-300 nm and *Å* (467, 660 nm) >1.5. By using ground-based nephelometer measurements, Yang et al. (2009) found that the biomass burning aerosol was characterized by a mean value of *Å* (450, 700 nm) equal to 1.52 near Beijing (China), while lower values (ranging from 0.8 to 1.5) were found by Lee et al. (2012) in Gosan (South Korea). Then, Aurélien et al. (2019) found from in situ measurements that the particles monitored during biomass-burning episodes were characterized in the turbulent layer by *Å* (450, 635 nm) = 1.8±0.3 (Table 4). Reid et al. (2005) have reviewed and discussed the literature concerning measurement and modelling of optical properties of biomass burning particles. They found that the most likely values of *g* for dry biomass-burning smoke at 550 nm vary within the 0.55-0.65 range. This last result is in good accordance with the corresponding BBN-*g* of this study (0.56 at 525 nm) and the ones (0.40 – 0.71 at 550 nm) found at a rural site in Leon (Spain) by Alonso-Blanco et al. (2014), as reported in Table 4. Reid et al. (2005) also estimated that the most likely values of mass scattering efficiency ($\Sigma_{PM10}$) for dry biomass-burning smoke at 550 nm range from 3.6 to 4.3, in good accordance with the related BBN- $\Sigma_{PM10}$ of this study (4.0 at 525 nm, Table 4). A larger mean value of $\Sigma_{PM10}$ (5.5 ± 0.5) was evaluated by McMeeking et al. (2005) during the Yosemite Aerosol Characterization Study that took place in Yosemite National Park from July to September 2002 to study the main effects of numerous wildfires active in the western United States.

The Ångström exponent associated with the SUL source (*Å*=1.54) also shows the dominant influence of fine-mode particles as the SUL-$\Delta\sigma_s$ value (41%) also suggests. However, the positive $\Delta Å$ value (0.24) indicates the effect of two separate particle modes likely contributing to the SUL source (Table 3). In fact, sulphate and ammonium, which are the main component of the SUL source, have two modes in the 0.1 to 1.0 μm size range (the condensation and droplet modes), and a third one over 1.0 μm (coarse mode), according to Seinfeld and Pandis (1998). The spectral dependence of the asymmetry parameter values of this study (Table 3) is in good accordance with the ones suggested by d'Almeida et al. (1991) for the sulphate aerosol, which are equal to 0.73 and 0.71 at 450 nm and 650 nm, respectively. The SUL-*g* parameter at 525 nm found at the study site (0.62) is also quite similar to the one at 550 nm (0.64) determined by Mallet et al. (2011) for sulphate particles monitored over the French Mediterranean coastal region (Table 4). The SUL mass scattering efficiency retrieved in this study (SUL-$\Sigma_{PM10}$ (525 nm) = 3.9 $m^2 g^{-1}$) is in satisfactory accordance with the value (3.7 ± 0.1 $m^2 g^{-1}$) obtained by Maring et al. (2000) over the Canary Islands (Spain) during July 1995. Hand and

Malm (2007) performed a survey of the ground-based estimates of aerosol mass scattering efficiencies for various aerosol species and size modes. In particular, applying a multilinear regression method to some ground-based measurements from different worldwide sites, they calculated a mean value of $\Sigma_{PM10}$ equal to 2.5 ± 0.6 $m^2 g^{-1}$ for sulphate particles, which is slightly lower than the one estimated in this study.

The Traffic (TRA) source, which is the dominant pollution source in SS (35.0%; Fig. 1c), is characterized by high contributions of both fine-mode combustion-related chemical species (mostly OC and EC) and coarse-mode road dust-related chemical species (mainly $Ca^{2+}$, Cr, Cu, Fe, and Mn), according to Chow (1995). Both the *Å* (0.96) and the *ΔÅ* (0.54) value also proved that coarse-mode particles play a significant role for the TRA source. The TRA-*Å* value is close to the one associated by Schmeisser et al. (2017) with "large-particle-BC-mixtures" observed at coastal or remote sites experiencing occasional sea salt, dust, biomass burning or pollution aerosol, as the monitoring site of this study (Table 4). In addition, Cappa et al. (2016) defined the "large particle/BC mix" cluster with *Å* (450-550 nm) lower than 1.5. Yu et al. (2019) found a mean value of *Å* (450-700 nm) equal to 0.99 (similar to that of this study equal to 0.96) during polluted periods affected by traffic particles in Nanjing (China) in January 2015. Conversely, larger mean values of *Å* (450, 700 nm) during pollution episodes that can be associated with the TRA source were found by Yang et al. (2009) near Beijing (China) and by Lee et al. (2012) in Gosan (South Korea). Observe from Table 3 that the TRA-*g* values vary rather weakly with the wavelength. In fact, Fiebig and Ogren (2006) have shown that the *g* dependence on the wavelength becomes weaker from particles characterized by diameters < 1 μm to the ones with diameters <10 μm and can even reverse in some cases. The increase of *g* with the wavelength is caused by the presence of two modes in the particle size range relevant for its calculation, accumulation and coarse mode, and is more pronounced when both modes are well separated. In this case, the scattering cross section of particles in the accumulation mode becomes small with respect to the contribution of the coarse mode particles when illuminated with longer wavelength radiation.

The ASS source (Table 3) is characterized by rather small daily averaged $\sigma_s$ values at all wavelengths and a negative *Å* value (-0.65). As suggested by Cermak et al. (2010), negative *Å* values could be an indication of reduced anthropogenic emissions with prevalence of coarse-mode particles. Singh et al. (2004) found that negative *Å* values and high aerosol optical depths were related to the transport of coarse-mode dust in northern India. In the Western Mediterranean basin, Pandolfi et al. (2011) found from the distribution of $\sigma_s$ at 635 nm as a function of the calculated *Å*(450, 635 nm) that negative *Å* values were always related to low scattering coefficients. Then, a closer analysis of the air mass origin revealed the absence of Saharan dust intrusions and the prevalence of Atlantic advection episodes

leading to low PM concentrations and scattering coefficients, in accordance with the results of this study (Table 4). Negative *Å* values varying from -0.35 to -0.09 have also been associated with marine particles monitored at the study site on 5 different days of February and March 2016, during the advection of air masses that crossed the Mediterranean Sea at very low altitudes before reaching Southeastern Italy (Romano et al., 2019a). Therefore, the negative ASS-*Å* value (-0.65) likely shows the significant contribution of coarse particles to the source. The small positive ASS-*ΔÅ* value (0.12) supports last comment, according to Schuster et al. (2006). The significant role of the coarse particle contribution in marine aerosol size distributions has been outlined in several studies (e.g., Seinfeld and Pandis, 1998). Costabile et al. (2013) in Rome (Italy) and Rivera et al. (2017) at the Cape San Juan Atmospheric Observatory (Puerto Rico) also found small values of ASS Ångström exponent (*Å* (467-660 nm) < 0.5 and *Å* (450-700 nm) = 0.33±0.18, respectively) that further prove the coarse mode particle contribution to marine aerosols. Pandolfi et al. (2018) investigated the scattering properties of atmospheric aerosol particles from 28 European sites and found that *g* did not show any clear gradient by station placement or geographical location, reflecting the complex relationship of this parameter with the physical properties of the aerosol particles. Note from Table 4 that the ASS-*g* (0.35 at 525 nm) of this study is lower than the corresponding values found by Horvath et al. (2018) in Granada (Spain) and by Fiebig and Ogren (2006) in Trinidad Head (California, USA). As previously reported in Section 3.2, *g* is generally higher for larger particles (as marine and/or dust aerosol) compared to fine particles (as anthropogenic aerosol) in most of the shortwave region. In addition, Fiebig and Ogren (2006) highlighted that the value of *g* can vary significantly with location and/or aerosol type. Accordingly, the three compared monitoring sites present different features. Lecce and Granada are both Mediterranean coastal sites typically characterized by a mixed aerosol type (desert dust from Northern Africa, polluted particles from urban and industrial areas of Northern and Eastern Europe, marine aerosols from the Mediterranean Sea and the Atlantic Ocean, and biomass burning particles from forest fires). However, these sites have specific features, since Lecce is a small-sized city located on a flat peninsular area away from large sources of local pollution (Section 2.1), while Granada is a medium-sized city surrounding by mountains (e.g., Titos et al., 2012; Horvath et al., 2018). On the contrary, Trinidad Head is a Pacific coastal site in Northern California and is mainly characterized by PM sources from the ocean, aged PM from sources in East Asia, pollution from shipping routes, and local emissions from the continental North America, as described in Allan et al. (2004). Hand and Malm (2007) used measurements performed aboard cruise platforms around the globe, assuming ideal collection efficiencies and apportioned size distributions, to derive average dry sea salt mass scattering efficiencies. They found that the average dry fine, coarse, and total sea salt mass scattering efficiencies at 550 nm are 4.5±0.7, 1.0±0.2, and 2.2±0.5 $m^2g^{-1}$, respectively. The

lower values associated with the coarse and total mode reflect the dominance of larger particles that are less efficient in light scattering, according to Hand and Malm (2007). They also performed multilinear regression analyses to estimate mass scattering efficiencies at 550 nm and found that the average coarse mode and total mass sea salt scattering efficiencies are 0.72±0.02 and 1.8±0.3 $m^2g^{-1}$, respectively. The mass scattering efficiencies reported by Hand and Malm (2007) for coarse sea salt particles are in satisfactory accordance with the one of this study (ASS-$\Sigma_{PM10}$ (at 525 nm) = 0.7 $m^2$ $g^{-1}$). In fact, the spectral dependence of $\sigma_s$ and $g$ and the $\AA$ and $\Delta\AA$ values reflect the significant role of coarse particles for the ASS source, as previously shown. Low ASS-$\Sigma_{PM}$ values were also estimated by Li et al. (1996) in Barbados and Chiapello et al. (1999) in Cape Verde (Table 4). A major missing piece of currently available aerosol classification methods is the identification and validation of optical property thresholds to classify sea salt particles, according to Schmeisser et al. (2017). Therefore, the results of this study combined with the ones of Romano et al. (2019a) have contributed to the intensive optical parameter characterization and, more specifically, to the identification and validation of the variability ranges of the optical properties associated with sea salt particles and/or sea salt sources at coastal sites.

*3.5 Case-study analyses*

Monitoring days in which a specific source was prevailing have been selected and analyzed in this subsection, to furtherly support the paper's results. PM10 mass concentrations and aerosol optical parameters have on average been affected by most of the PMF-identified pollution sources on each monitoring day, even if the percentage contribution of each pollution source varied day-by-day. The geographical location of the receptor site, which is away from large pollution sources, but it is impacted by long-range transported particles, contributed to this last result, as reported in previous studies (e.g., Perrone et al., 2013a; 2014; 2016; 2019a). Therefore, the comparison of the $\AA$, $\Delta\AA$, and $g$ values calculated from the $\sigma_s$ and $\beta_s$ values measured on the monitoring day, in which a pollution source was prevailing, with the corresponding intensive optical parameters associated by PMF with the prevailing pollution source could represent a good tool to further proving the reliability of the used methodology. Figure SM3, which shows the daily-mean time evolution of (a) $\sigma_s$ (450 nm) and (b) PM10 mass concentrations day-by-day associated with the pollution sources, has been used to identify monitoring days with a prevailing pollution source. Figure SM3 shows that the BBN source was prevailing on 1st December 2011, the TRA source was prevailing on 31 August 2012, while the ASS source was prevailing on 5 April 2012. A day in which the SUL source was by far the largest one has not been identified in the dataset of this study.

### *3.5.1 Case-study: 1st December 2011*

The BBN source was by far the largest pollution source on 1st December 2011 (Fig. SM3), since the PMF BBN-$\sigma_s$ and -PM10 values represented 82 and 77% of the total $\sigma_s$ and PM10 daily means, respectively, reconstructed by PMF (Table 5). Figure 4a shows by a bar plot the mass percentage of the monitored chemical species on 1st December 2011, where *Met* represents the mass percentage of all tested metals (Al, Cr, Cu, Fe, Mn, and Ti), *Sea* the one due to $Na^+$ and $Cl^-$, and *Sul* the one due to $SO_4^{2-}$ and $NH_4^+$. Note that the mass percentage due to OC, EC, $K^+$, and $NO_3^-$, which are the main tracers of the BBN source, represents about 60% of the sampled PM10 mass (Fig. 4a). The PM10 and $\sigma_s$ percentages associated by PMF with the identified pollution sources are shown by a bar plot in Fig. 4b and 4c, respectively, to highlight the relationship between the PM10 and $\sigma_s$ source apportionment and the sample chemical composition. Figures 4b and 4c are rather similar because of the rather high value of the BBN mass scattering efficiency (Table 3). Table 5 shows the experimentally determined PM10, $\sigma_s$ (450 nm), $\mathring{A}$, $\Delta\mathring{A}$, and $g$(450 nm) daily means (± SEM) on 1st December 2011 and the corresponding values associated by PMF with the BBN pollution sources. The total reconstructed PMF-$\sigma_s$ (at 450 nm) is 10% smaller, and the reconstructed PMF-PM10 and -$\beta_s$ (at 450 nm) values are 20% and 7% greater, respectively, than the corresponding experimental daily means. The differences between the intensive optical parameters $\mathring{A}$, $\Delta\mathring{A}$, and $g$ associated by PMF with the BBN source and the corresponding experimental parameters of 1st December 2011 are even smaller (Table 5). Besides supporting the reliability of the intensive optical parameters associated by PMF with the BBN source, these last results also support the methodology used in this study.

Figure SM4 shows the four-day analytical backtrajectories reaching the study site at 270, 500, and 1000 m above ground level (AGL) on 1st December 2011 at 12:00 UTC, by the Hybrid Single Particle Lagrangian Integrated Trajectory (HYSPLIT) model version 4.8, from NOAA/ARL (Draxler and Hess, 1998). Observe that the 270 and 500 m arrival height backtrajectories crossed north-eastern European countries at very low altitudes before reaching the study site. Therefore, they have likely contributed to the advection of BBN particles to the monitoring site, in accordance with previous studies (Perrone et al., 2014; Romano 2019a). Note that the combined analysis of backtrajectories and nephelometer measurements performed from December 2011 to November 2012 (Perrone et al., 2014) has shown that north-eastern (NE) advection patterns were on average responsible at the study site for the highest and smallest $\mathring{A}$ and $\Delta\mathring{A}$ daily means, in satisfactory accordance with the finding of this study (Table 5). In conclusion, considering these last results and the back-trajectories analysis, we believe that the estimated values of $\mathring{A}$, $\Delta\mathring{A}$, and $g$ of this case study can be considered as typical of the BBN source at the study site.

### 3.5.2 Case-study: 31 August 2012

The TRA source was by far the prevailing one on 31 August 2012. In fact, the PMF TRA-$\sigma_s$ and -PM10 values represents 71 and 67% of the total $\sigma_s$ and PM10 values, respectively, reconstructed by PMF (Table 5). Moreover, the PMF reconstructed PM10, $\sigma_s$(450 nm) and $\beta_s$(450 nm) values, which are in satisfactory accordance with the corresponding experimental values, support the PMF retrievals on 31 August 2012 (Table 5). Figure 5 shows by bar plots the (a) mass percentage of the monitored chemical species and (b) PM10, and (c) $\sigma_s$ percentages associated with the identified pollution sources. The mass percentage associated with the TRA source is dominated by the one related to OC and EC, which corresponds to ~71% of the total sampled PM10 mass. The remaining mass percentage (~2%) related to the TRA source can be associated with its typical trace elements like $Ca^{2+}$, Cr, Cu, Fe, and Mn. The percentage differences between the experimental $\mathring{A}$, $\Delta\mathring{A}$, and $g$(450 nm) daily means and the corresponding values associated with the TRA source are equal to 6, 22, and 5%, respectively. Figure SM5 shows the HYSPLIT four-day analytical backtrajectories reaching the study site at 270, 500, and 1000 m above ground level (AGL) on 31 August 2012 at 12:00 UTC. In accordance with Perrone et al. (2014; Figure 7), the backtrajectory pathways may be associated with the slow-North-West (slowNW) centroid that is generally associated with polluted conditions. Perrone et al. (2014) have also shown that the $\sigma_s$(450 nm), $\beta_s$(450 nm), and $\mathring{A}$ mean values associated with slowNW air flows were on average slightly smaller than the corresponding values associated with NE advections, as shown by the comparison of the optical parameter values of 31 August 2012 with the corresponding ones of 1st December 2011. Table 5 shows that the experimentally determined $\mathring{A}$ and $\Delta\mathring{A}$ mean values indicate that the contribution of coarse mode particles was on 31 August 2012 greater than that of 1st December 2011. In conclusion, we believe that the results reported in this sub-section indicate the estimated values of the intensive optical parameters $\mathring{A}$, $\Delta\mathring{A}$, and $g$ as typical of the TRA source at the study site.

### 3.5.3 Case-study: 5 April 2012

The ASS source was by far the prevailing one on 5 April 2012, according to the ASS-PM10 mass concentration, which represents 68% of the total one reconstructed by PMF. In contrast, the ASS-$\sigma_s$ value represents only 37% of the total $\sigma_s$ reconstructed by PMF (Table 5) because of the weak sensitivity of $\sigma_s$(450 nm) to the coarse particles mainly contributing to the ASS source (e.g., Seinfeld and Pandis, 1998). Figure 6 shows by bar plots (a) the mass percentage of the monitored chemical species and (b) PM10 and (c) $\sigma_s$ percentages associated with the identified pollution sources. The

mass percentage related to the ASS source, whose main tracers are $Na^+$, $Cl^-$, and $Mg^{2+}$, represents about 20% of the total sampled mass. However, we must be aware that the undetermined mass accounts for about 45% on 5 April, likely because of the greater contribution of unmonitored/ undetected chemical species and/or bioaerosols (e.g., Fröhlich-Nowoisky et al., 2016; Romano et al., 2019b) than on the previous case studies. Figure 6b shows that the ASS-PM10 mass accounts for about 68% of the total reconstructed PM10 mass and that the BBN-PM10 mass accounts for about 14%. The BBN source was the second most abundant source on 5 April 2012 (Table 5). Then, Figure 6c shows that BBN- and ASS-$\sigma_s$ account for 63% and 37% of the total reconstructed $\sigma_s$, respectively, since the mass scattering efficiency associated with BBN particles is more than 5 times greater than the one associated with ASS particles (Table 3). Fine and coarse particles, which are characterized by different $\sigma_s$ spectral dependence, dominate the BBN- and the ASS-source, respectively (e.g., Seinfeld and Pandis, 1998). Consequently, the differences between the intensive optical parameters ASS-$\mathring{A}$, -$\Delta\mathring{A}$, and -$g$ and the corresponding experimental values of 5 April 2012 are greater than in the previous two analyzed case studies (Table 5). The BBN particle contribution on 5 April 2012 has likely significantly affected the size distribution of the monitored atmospheric particles and, hence, their scattering properties. Therefore, Table 5 likely shows that the intensive optical properties associated with an aerosol mixture, like the (BBN+ASS) aerosol mixture, can be rather different from the ones determined by the percentage contribution of each source. In fact, Cappa et al. (2016) and Romano et al. (2019a) at the study site have shown that the intensive optical parameters associated with a specific aerosol mixture on average spread over a wide range of values. In fact, the scattering properties of an aerosol mixture may significantly change with the percentage contribution of each component.

Figure SM6 shows the HYSPLIT four-day analytical backtrajectories that reach the study site at 270, 500, and 1000 m above ground level (AGL) on 5 April 2012 at 12:00 UTC. The backtrajectory pathways that crossed the eastern Mediterranean Sea, close to the sea surface, before reaching the study site, support the significant advection of sea-salt particles.

### *3.5.4 Comments on PMF and experimental result differences in the selected case studies*

PMF-estimated and experimental total PM10 mass concentrations and optical parameters (scattering coefficient $\sigma_s$, backscattering coefficient $\beta_s$, Ångström exponent $\mathring{A}$, Ångström exponent difference $\Delta\mathring{A}$, and asymmetry parameter $g$) have been reported in Table 5 for the three selected case studies discussed in the previous subsections. PM10 concentrations and optical parameter values estimated by PMF for the Traffic (TRA), Biomass Burning + Nitrates (BBN), Soil Dust (SDU), ammonium Sulphate (SUL), and Aged Sea-salt (ASS) pollution sources have also been given in Table 5 to

highlight the impact of each source in the selected monitoring days. Data referring to the prevailing pollution source, according to the PM10 mass reconstruction, are in bold in Table 5. As mentioned, the accordance between experimental and PMF results was rather satisfactory on 1st December 2011, supporting the PMF assignment of the intensive optical parameters $\AA$, $\Delta\AA$, and $g$ values to the BBN source. The quite high impact of the BBN source on 1st December contributed to this result. The BBN-$\sigma_s$ and -PM10 values represented 82 and 77% of the total $\sigma_s$ and PM10 daily means, respectively, reconstructed by PMF.

The TRA-$\sigma_s$ and -PM10 values represented 71 and 67% of the total $\sigma_s$ and PM10 values, respectively, reconstructed by PMF on 31 August 2012. The percentage differences between the experimental $\AA$, $\Delta\AA$, and $g$(450 nm) daily means and the corresponding values associated with the TRA source, which are equal to 6, 22, and 5%, respectively, are satisfactory. However, we must be aware that several pollution sources played a significant role on 31 August 2012, representing 29 and 33% of the PMF reconstructed PM10 and $\sigma_s$(450 nm) values, respectively. Therefore, we believe that the PMF retrievals of 31 August 2012 can also support the PMF assignment of the intensive optical parameters $\AA$, $\Delta\AA$, and $g$ values to the TRA source.

The ASS source was by far the prevailing one on 5 April 2012, according to the ASS-PM10 mass concentration, which represented 68% of the total one reconstructed by PMF. However, Table 5 shows that the percentage differences between the experimental $\AA$, $\Delta\AA$, and $g$(450 nm) daily means and the corresponding values associated with the ASS source are larger than the ones found in the previous case studies. The significant role of the BBN source and the large percentage of the undetermined mass (45%) on 5 April contributed to this last result, as discussed in the previous subsection.

We believe that the above analyses have clearly shown that the experimentally determined $\AA$, $\Delta\AA$, and $g$ values were in good accordance with the corresponding parameters associated by the PMF, mainly with a prevailing pollution source. The significant impact of the long-range advected air masses at the receptor site has also been highlighted in this last intercomparison analysis.

## 4 Summary and conclusion

A PMF source apportionment analysis has been performed by integrating chemically speciated PM10 mass concentrations and corresponding extensive optical properties, with the main goal of associating intensive optical parameters with the identified pollution sources.

- A 5-factor PMF solution has been the most physically robust one.

● The source apportionment of the PM10 mass considering the whole dataset (from November 2011 to November 2012) was: traffic (28%), biomass burning+nitrate (27%), soil dust (15%), ammonium sulphate (17%), and aged sea-salt (13%). In contrast, the source apportionment of the scattering coefficient at 450 nm was: traffic (30%), biomass burning+nitrate (42%), soil dust (0%), ammonium sulphate (26%), and aged sea-salt (2%). Most probably, the differences were mainly due to the weak sensitivity of the scattering coefficient to coarse mode particles.

● PM10 and $\sigma_s$(450 nm) source apportionment assumed a similar seasonal dependence. BBN source prevailed in AW, while TRA source was predominant in SS. ASS source presented a weakly seasonal-dependence.

● The scattering efficiency by small particles reached the maximum value when the size parameter was comparable with the monitoring wavelength. Therefore, the need of optimizing the $\sigma_s$ monitoring wavelength to characterize pollution sources where coarse particles are prevailing has been outlined.

• The $\mathring{A}$ (1.57) and $\Delta\mathring{A}$ (-0.06) values associated with the BBN source indicate a dominance of a single small particle mode. The $\mathring{A}$ (1.54) value shows the dominant influence of fine-mode particles for the SUL source. Both the $\mathring{A}$ (0.96) and $\Delta\mathring{A}$ (0.54) values show the significant role of the coarse mode particles associated with the TRA source, in addition to the fine particle contribution. The negative $\mathring{A}$ value (-0.65) and the positive $\Delta\mathring{A}$ value (0.12) show that the contribution of coarse mode particles to the ASS source was the largest among the studied sources.

• The PM10 mass scattering efficiency at 450 nm was equal to 5.0 $m^2g^{-1}$ for both the BBN and the SUL sources. $\Sigma_{PM10}$ values associated with TRA and ASS sources were lower (3.4 and 0.6 $m^2g^{-1}$, respectively), proving its decreasing trend with the increase of the coarse particle contribution.

• We have found that the highest asymmetry parameter *g* value at 450 nm (0.67) was associated with the SUL source. The *g*(450 nm) values associated with the BBN and TRA sources were equal to 0.58 and 0.57, respectively, and decreased down to 0.34 for the ASS source.

In conclusion, paper's results have shown the ability of the proposed methodology to characterize pollution sources by intensive optical parameters ($\mathring{A}$, $\Delta\mathring{A}$, $\Sigma_{PM10}$, and *g*). The comparison of the paper's results with literature values and the analysis of monitoring days with a prevailing pollution source have also proved the reliability of the used methodology. In addition, this paper has also contributed to the characterization of the marine particle optical properties, which represents a major missing piece of the current aerosol classification methods.

We believe that the paper's results can be of general interest for the scientific community, since the suggested methodology can contribute to the identification and validation of optical parameters associated with typical pollution sources of Central Mediterranean coastal sites away from large sources of local pollution.

**Acknowledgments**

S. Romano has carried out this work with the support of a postdoctoral fellowship from the Consorzio Nazionale Interuniversitario per le Scienze fisiche della Materia (CNISM). The financial support of EARLINET as part of the ACTRIS Research Infrastructure Project by the European Union's Horizon 2020 research and innovation programme under grant agreement no. 654169 (previously under grant agreement no. 262254) in the 7th Framework Programme (FP7/2007-2013) is gratefully acknowledged. A. Genga from Dipartimento di Scienze e Tecnologie Biologiche ed Ambientali, Università del Salento, Lecce (Italy) is kindly acknowledged for the ion and metal analyses of the PM10 samples. The NOAA Air Resources Laboratory is kindly acknowledged for the provision of the HYSPLIT back trajectories.

## References


Allan, J.D., Bower, K.N., Coe, H., Boudries, H., Jayne, J.T., Canagaratna, M.R., Millet, D.B., Goldstein, A.H., Quinn, P.K., Weber, R.J., Worsnop, D.R., 2004. Submicron aerosol composition at Trinidad Head, California, during ITCT 2K2: Its relationship with gas phase volatile organic carbon and assessment of instrument performance. J. Geophys. Res., 109, D23S24. DOI: 10.1029/2003JD004208.

Alonso-Blanco, E., Calvo, A.I., Pont, V., Mallet, M., Fraile, R., Castro, A., 2014. Impact of Biomass Burning on Aerosol Size Distribution, Aerosol Optical Properties and Associated Radiative Forcing. Aerosol Air Qual. Res. 14, 708-724. DOI: 10.4209/aaqr.2013.05.0163.

Andreae, T.W., Andreae, M.O., Ichoku, C., Maenhaut, W., Cafmeyer, J., Karnieli, A., Orlovsky, L., 2002. Light scattering by dust and anthropogenic aerosol at a remote site in the Negev desert, Israel. J. Geophys. Res. 107(D2). DOI: 10.1029/2001JD900252.

Andrews, E., Sheridan, P.J., Fiebig, M., McComiskey, A., Ogren, J.A., Arnott, P., Covert, D., Elleman, R., Gasparini, R., Collins, D., Jonsson, H., Schmid, B., Wang, J., 2006. Comparison of methods for deriving aerosol asymmetry parameter. J. Geophys. Res. 111, D05S04. DOI: 10.1029/2004JD005734.

Aurélien, C., Aliaga, D., Andrade, M., Ginot, P., Krejci, R., Močnik, G., Montoux, N., Moreno, I., Müller, T., Pandolfi, M., Sellegri, K., Velarde, F., Wiedensohler, A., Weinhold, K., Laj, P., 2019. Biomass-burning and urban emission impacts in the Andes Cordillera region based on in-situ measurements from the Chacaltaya observatory, Bolivia (5240 m a.s.l.). Atmos. Chem. Phys. Discuss. DOI: 10.5194/acp-2019-510.

Bergamo, A., Tafuro, A.M., Kinne, S., De Tomasi, F., Perrone, M.R., 2008. Monthly-averaged anthropogenic aerosol direct radiative forcing over the Mediterranean based on AERONET aerosol properties. Atmos. Chem. Phys. 8, 6995-7014. DOI: 10.5194/acp-8-6995-2008.

Birch, M.E., Cary, R.A., 1996. Elemental carbon-based method for monitoring occupational exposures to particulate diesel exhaust. Aerosol Sci. Technol. 25, 221-241. DOI: 10.1080/02786829608965393.

Cappa, C.D., Kolesar, K.R., Zhang, X., Atkinson, D.B., Pekour, M.S., Zaveri, R.A., Zelenyuk, A., Zhang, Q., 2016. Understanding the optical properties of ambient sub- and supermicron particulate matter: results from the CARES 2010 field study in northern California. Atmos. Chem. Phys. 16, 6511-6535. DOI: 10.5194/acp-16-6511-2016.

Cermak, J., Wild, M., Knutti, R., Mishchenko, M.I., Heidinger, A.K., 2010. Consistency of global satellite-derived aerosol and cloud data sets with recent brightening observations. Geophys. Res. Lett. 37, L21704. DOI: 10.1029/2010GL044632.

Charlson, R.J., Schwartz, S.E., Hales, J.M., Cess, R.D., Coakley, J.A., Hansen, J., Hofmann, D.J., 1992. Climate forcing by anthropogenic aerosols. Science 255, 423-430. DOI: 10.1126/science.255.5043.423.

Chiapello, I., Bergametti, G., Chatenet, B., Dulac, F., Jankowiak, I., Liousse, C., Soares, E.S., 1999. Contribution of the different aerosol species to the aerosol mass load and optical depth over the northeastern tropical Atlantic. J. Geophys. Res. 104 (D4), 4025-4035. DOI: 10.1029/1998JD200044.

Chow, J.C., 1995. Measurement Methods to Determine Compliance with Ambient Air Quality Standards for Suspended Particles. J. Air Waste Manag. Assoc. 45, 320-382. DOI: 10.1080/10473289.1995.10467369.

Clarke, A., Kapustin, V., 2010. Hemispheric aerosol vertical profiles: anthropogenic impacts on optical depth and cloud nuclei. Science 329, 1488-1492. DOI: 10.1126/science.1188838.

Costabile, F., Barnaba, F., Angelini, F., Gobbi, G. P., 2013. Identification of key aerosol populations through their size and composition resolved spectral scattering and absorption. Atmos. Chem. Phys. 13, 2455-2470. DOI: 10.5194/acp-13-2455-2013.

Costabile, F., Gilardoni, S., Barnaba, F., Di Ianni, A., Di Liberto, L., Dionisi, D., Manigrasso, M., Paglione, M., Poluzzi, V., Rinaldi, M., Facchini, M.C., Gobbi, G.P., 2017. Characteristics of brown carbon in the urban Po Valley atmosphere. Atmos. Chem. Phys. 17, 313-326. DOI: 10.5194/acp-17-313-2017.

D'Almeida, G.A., Keopke, P., Shettle, E.P., 1991. Atmospheric Aerosol: Global Climatology and Radiative Characteristics. A. Deepak Publishing, Hampton, VA.

Denjean, C., Cassola, F., Mazzino, A., Triquet, S., Chevaillier, S., Grand, N., Bourrianne, T., Momboisse, G., Sellegri, K., Schwarzenbock, A., Freney, E., Mallet, M., Formenti, P., 2016. Size distribution and optical properties of mineral dust aerosols transported in the western Mediterranean. Atmos. Chem. Phys. 16, 1081-1104. DOI: 10.5194/acp-16-1081-2016.

Draxler, R.R., Hess, G.D., 1998. An overview of the HYSPLIT_4 modeling system of trajectories, dispersion, and deposition. Aust. Meteorol. Mag. 47, 295-308.

Ealo, M., Alastuey, A., Ripoll, A., Pérez, N., Minguillón, M.C., Querol, X., Pandolfi, M., 2016. Detection of Saharan dust and biomass burning events using near-real-time intensive aerosol optical properties in the north-western Mediterranean. Atmos. Chem. Phys. 16, 12567-12586. DOI: 10.5194/acp-16-12567-2016.

Fernández, A.J., Molero, F., Salvador, P., Revuelta, A., Becerril-Valle, M., Gómez-Moreno, F.J., Artíñano, B., Pujadas, M., 2017. Aerosol optical, microphysical and radiative forcing properties during variable intensity African dust events in the Iberian Peninsula. Atmos. Res. 196, 129-141. DOI: 10.1016/j.atmosres.2017.06.019.

Fiebig, M., Ogren, J.A., 2006. Retrieval and climatology of the aerosol asymmetry parameter in the NOAA aerosol monitoring network. J. Geophys. Res. 111, D21204. DOI:10.1029/2005JD006545.

Forello, A.C., Bernardoni, V., Calzolai, G., Lucarelli, F., Massabò, D., Nava, S., Pileci, R.E., Prati, P., Valentini, S., Valli, G., Vecchi, R., 2019. Exploiting multi-wavelength aerosol absorption coefficients in a multi-time resolution source apportionment study to retrieve source-dependent absorption parameters. Atmos. Chem. Phys. 19, 11235-11252. DOI: 10.5194/acp-19-11235-2019.

Fröhlich-Nowoisky, J., Kampf, C.J., Weber, B., Huffman, J.A., Pöhlker, C., Andreae, M.O., Lang-Yona, N., Burrows, S.M., Gunthe, S.S., Elbert, W., Su, H., Hoor, P., Thines, E., Hoffmann, T., Després, V.R., Pöschl, U., 2016. Bioaerosols in the earth system: climate, health, and ecosystem interactions. Atmos. Res. 182, 346-376. DOI: 10.1016/j.atmosres.2016.07.018.

Hand, J.L., Malm, W.C., 2007. Review of aerosol mass scattering efficiencies from ground-based measurements since 1990. J. Geophys. Res. 112, D16203. DOI: 10.1029/2007JD008484.

Haywood, J.M., Ramaswamy, V., 1998. Global sensitivity studies of the direct radiative forcing due to anthropogenic sulfate and black carbon aerosols. J. Geophys. Res. 103, 6043-6058. DOI: 10.1029/97JD03426.

Hopke, P.K., 2016. Review of receptor modeling methods for source apportionment. J. Air Waste Manage. 66 (3), 237-259. DOI: 10.1080/10962247.2016.1140693.

Horvath, H., Alados Arboledas, L., Olmo Reyes, F.J., 2018. Angular scattering of the Sahara dust aerosol. Atmos. Chem. Phys. 18, 17735-17744. DOI: 10.5194/acp-18-17735-2018.

Huang, K., Zhuang, G., Lin, Y., Li, J., Sun, Y., Zhang, W., Fu, J.S., 2010. Relation between optical and chemical properties of dust aerosol over Beijing, China. J. Geophys. Res. 115, D00K16. DOI: 10.1029/2009JD013212.

Kaufman, Y.J., 1993. Aerosol optical thickness and atmospheric path radiance. J. Geophys. Res. 98 (D2), 2677-2692. DOI: 10.1029/92JD02427.

Kim, E., Hopke, P.K., 2007. Source identifications of airborne fine particles using positive matrix factorization and U.S. Environmental Protection Agency positive matrix factorization. J. Air Waste Manag. Assoc. 57(7), 811-819. DOI: 10.3155/1047-3289.57.7.811.

Kokhanovsky, A.A., 2008. Aerosol optics – Light Absorption and Scattering by Particles in the Atmosphere. Springer Praxis Books, Springer Berlin Heidelberg, 148 pp.

Latimer, R.N.C., Martin, R.V., 2019. Interpretation of measured aerosol mass scattering efficiency over North America using a chemical transport model. Atmos. Chem. Phys. 19, 2635-2653. DOI: 10.5194/acp-19-2635-2019.

Lee, S., Yoon, S.C., Kim, S.W., Kim, Y.P., Ghim, Y.S., Kim, J.H., Kang, C.H., Kim, Y.J., Chang, L.S., Lee, S.J., 2012. Spectral dependency of light scattering/absorption and hygroscopicity of pollution and dust aerosols in Northeast Asia. Atmos. Environ. 50, 246-254. DOI: 10.1016/j. atmosenv.2011.12.026.

Li, X., Maring, H., Savoie, D., Voss, K., Prospero, J.M., 1996. Dominance of mineral dust in aerosol light-scattering in the North Atlantic trade winds. Nature 380, 416-419. DOI: 10.1038/380416a0.

Lohmann, U., Feichter, J., 2005. Global indirect aerosol effects: a review. Atmos. Chem. Phys. 5, 715-737. DOI: 10.5194/acp-5-715-2005.

Lopatin, A., Dubovik, O., Chaikovsky, A., Goloub, P., Lapyonok, T., Tanré, D., Litvinov, P., 2013. Enhancement of aerosol characterization using synergy of lidar and sun-photometer coincident observations: the GARRLiC algorithm. Atmos. Meas. Tech. 6, 2065-2088. DOI: 10.5194/amt-6-2065-2013.

Mallet, M., Roger, J.C., Despiau, S., Dubovik, O., Putaud, J.P., 2003. Microphysical and optical properties of aerosol particles in urban zone during ESCOMPTE. Atmos. Res. 69, 73-97. DOI: 10.1016/j.atmosres.2003.07.001.

Mallet, M., Gomes, L., Solmon, F., Sellegri, K., Pont, V., Roger, J.C., Missamou, T., Piazzola, J., 2011. Calculation of key optical properties of the main anthropogenic aerosols over the Western French coastal Mediterranean Sea. Atmos. Res. 101, 396-411. DOI: 10.1016/j.atmosres.2011. 03.008.

Maring, H., Savoie, D.L., Izaguirre, M.A., McCormick, C., Arimoto, R., Prospero, J.M., Pilinis, C., 2000. Aerosol physical and optical properties and their relationship to aerosol composition in the

free troposphere at Izaña, Tenerife, Canary Islands, during July 1995. J. Geophys. Res. 105(D11), 14677-14700. DOI: 10.1029/2000JD900106.

McMeeking, G.R., Kreidenweis, S.M., Carrico, C.M., Lee, T., Collett Jr., J.L., Malm, W.C., 2005. Observations of smoke-influenced aerosol during the Yosemite Aerosol Characterization Study: Size distributions and chemical composition. J. Geophys. Res. 110, D09206. DOI: 10.1029/2004 JD005389.

Minguillòn, M.C., Querol, X., Baltensperger, U., Prevot, A.S.H., 2012. Fine and Coarse PM Composition and Sources in Rural and Urban Sites in Switzerland: Local or Regional Pollution? Sci. Total Environ. 427-428, 191-202. DOI: 10.1016/j.scitotenv.2012.04.030.

Müller, T., Henzing, J.S., de Leeuw, G., Wiedensohler, A., 2011. Design and performance of a three-wavelength LED-based total scatter and backscatter integrating nephelometer. Atmos. Meas. Tech. 4, 1291-1303. DOI: 10.5194/amt-4-1291-2011.

Nicolás, J.F., Castañer, R., Crespo, J., Yubero, E., Galindo, N., Pastor, C., 2018. Seasonal variability of aerosol absorption parameters at a remote site with high mineral dust loads. Atmos. Res. 210, 100-109. DOI: 10.1016/j.atmosres.2018.04.008

Nicolás, J.F., Castañer, R., Galindo, N., Yubero, E., Crespo, J., Clemente, A., 2019. Analysis of aerosol scattering properties and $PM_{10}$ concentrations at a mountain site influenced by mineral dust transport. Atmos. Environ. 213, 250-257. DOI: 10.1016/j.atmosenv.2019.06.017.

NIOSH, 1999. Method 5040 Issue 3 (Interim): Elemental Carbon (Diesel Exhaust). In NIOSH Manual of Analytical Methods. National Institute of Occupational Safety and Health, Cincinnati, OH.

Norris, G., Duvall, R., Brown, S., Bai, S., 2014. EPA Positive Matrix Factorization (PMF) 5.0 fundamentals and user guide. Prepared for the U.S. Environmental Protection Agency Office of Research and Development, Washington, DC, EPA/600/R-14/108.

Nousiainen, T., Kandler, K., 2015. Light scattering by atmospheric mineral dust particles. In: Light Scattering Reviews 9, edited by: Kokhanovsky, A.A., Springer Praxis Books, Springer, Berlin, Heidelberg, 3-52. DOI: 10.1007/978-3-642-37985-7.

O'Neill, N.T., Eck, T.F., Smirnov, A., Holben, B.N., Thulasiraman, S., 2003. Spectral discrimination of coarse and fine mode optical depth. J. Geophys. Res. 108, 4559. DOI: 10.1029/2002JD002975.

Paatero, P., 2015. User's Guide for Positive Matrix Factorization Programs PMF2 and PMF3, Part 1-2: Tutorial. University of Helsinki: Helsinki, Finland (update 31 March 2015).

Paatero, P., Tapper, U., 1994. Positive matrix factorization: A non-negative factor model with optimal utilization of error estimates of data values. Environmetrics 5, 111-126. DOI:10.1002/env.3170050203.

Pandolfi, M., Cusack, M., Alastuey, A., Querol, X., 2011. Variability of aerosol optical properties in the Western Mediterranean Basin. Atmos. Chem. Phys. 11, 8189-8203. DOI: 10.5194/acp-11-8189-2011.

Pandolfi, M., Alados-Arboledas, L., Alastuey, A., Andrade, M., Angelov, C., Artiñano, B., Backman, J., Baltensperger, U., Bonasoni, P., Bukowiecki, N., Collaud Coen, M., Conil, S., Coz, E., Crenn, V., Dudoitis, V., Ealo, M., Eleftheriadis, K., Favez, O., Fetfatzis, P., Fiebig, M., Flentje, H., Ginot, P., Gysel, M., Henzing, B., Hoffer, A., Holubova Smejkalova, A., Kalapov, I., Kalivitis, N., Kouvarakis, G., Kristensson, A., Kulmala, M., Lihavainen, H., Lunder, C., Luoma, K., Lyamani, H., Marinoni, A., Mihalopoulos, N., Moerman, M., Nicolas, J., O'Dowd, C., Petäjä, T., Petit, J.-E., Pichon, J. M., Prokopciuk, N., Putaud, J.-P., Rodríguez, S., Sciare, J., Sellegri, K., Swietlicki, E., Titos, G., Tuch, T., Tunved, P., Ulevicius, V., Vaishya, A., Vana, M., Virkkula, A., Vratolis, S., Weingartner, E., Wiedensohler, A., Laj, P., 2018. A European aerosol phenomenology – 6: scattering properties of atmospheric aerosol particles from 28 ACTRIS sites. Atmos. Chem. Phys. 18, 7877-7911. DOI: 10.5194/acp-18-7877-2018.

Pauraite, J., Plauškaitė, K., Dudoitis, V., Ulevicius, V., 2018. Relationship between the Optical Properties and Chemical Composition of Urban Aerosol Particles in Lithuania. Adv. Meteorol., 8674173. DOI: 10.1155/2018/8674173.

Perrone, M.R., Carofalo, I., Dinoi, A., Buccolieri, A., Buccolieri, G., 2009. Ionic and elemental composition of TSP, PM10, and PM2.5 samples collected over South-East Italy. Il Nuovo Cimento B 124, 341-356. DOI: 10.1393/ncb/i2009-10770-2.

Perrone, M.R., Piazzalunga, A., Prato, M., Carofalo, I., 2011. Composition of fine and coarse particles in a coastal site of the central Mediterranean: Carbonaceous species contributions. Atmos. Environ. 45(39), 7470-7477. DOI: 10.1016/j.atmosenv.2011.04.030.

Perrone, M., Becagli, S., Garcia Orza, J.A.G., Vecchi, R., Dinoi, A., Udisti, R., Cabello, M., 2013a. The impact of long-range-transport on PM1 and PM2.5 at a Central Mediterranean site. Atmos. Environ. 71, 176-186. DOI: 10.1016/j.atmosenv.2013.02.006.

Perrone, M.R., Dinoi, A., Becagli, S., Udisti, R., 2013b. Chemical composition of PM1 and PM2.5 at a suburban site in southern Italy. Int. J. Environ. An. Ch. 94, 127-150. DOI: 10.1080/03067319.2013.791978.

Perrone, M.R., Romano, S., Orza, J.A.G., 2014. Particle optical properties at a Central Mediterranean site: Impact of advection routes and local meteorology. Atmos. Res. 145-146, 152-167. DOI: 10.1016/j.atmosres.2014.03.029.

Perrone, M.R., Burlizzi, P., 2015. Methodologies to obtain aerosol property profiles from three-wavelength elastic lidar signals. Int. J. Remote Sens. 36, 4748-4773. DOI: 10.1080/01431161.2015.1093193.

Perrone, M.R., Romano, S., Orza, J.A.G., 2015. Columnar and ground-level aerosol optical properties: sensitivity to the transboundary pollution, daily and weekly patterns, and relationships. Environ. Sci. Pollut. R. 22, 16570-16589. DOI: 10.1007/s11356-015-4850-7.

Perrone, M.R., Genga, A., Siciliano, M., Siciliano, T., Paladini, F., Burlizzi, P., 2016. Saharan dust impact on the chemical composition of PM10 and PM1 samples over south-eastern Italy. Arab. J. Geosci. 9, 127. DOI: 10.1007/s12517-015-2227-3.

Perrone, M.R., Romano, S., Genga, A., Paladini, F., 2018. Integration of optical and chemical parameters to improve the particulate matter characterization. Atmos. Res. 205, 93-106. DOI: 10.1016/j.atmosres.2018.02.015.

Perrone, M.R., Vecchi, R., Romano, S., Becagli, S., Traversi, R., Paladini, F., 2019a. Weekly cycle assessment of PM mass concentrations and sources, and impacts on temperature and wind speed in Southern Italy. Atm. Res. 218, 129-144. DOI: 10.1016/j.atmosres.2018.11.013.

Perrone, M.R., Bertoli, I., Romano, S., Russo, M., Rispoli, G., Pietrogrande, M.C., 2019b. PM2.5 and PM10 oxidative potential at a Central Mediterranean Site: Contrasts between dithiothreitol- and ascorbic acid-measured values in relation with particle size and chemical composition. Atmos. Environ. 210, 143-155. DOI: 10.1016/j.atmosenv.2019.04.047.

Pietrogrande, M.C., Manarini, F., Perrone, M.R., Udisti, R., Romano, S., Becagli, S., 2018. PM10 Oxidative Potential at a Central Mediterranean Site: Association with Chemical Composition and Meteorological Parameters. Atmos. Environ. 188, 97-111. DOI: 10.1016/j.atmosenv.2018.06.013.

Polissar, A.V., Hopke, P.K., Paatero, P., Malm, W.C., Sisler, J.F., 1998. Atmospheric Aerosol over Alaska: 2. Elemental Composition and Sources. J. Geophys. Res. 103, 19045-19057. DOI: 10.1029/98JD01212.

Querol, X., Alastuey, A., Pey, J., Cusack, M., Pérez, N., Mihalopoulos, N., Theodosi, C., Gerasopoulos, E., Kubilay, N., Koçak, M., 2009. Variability in regional background aerosols within the Mediterranean. Atmos. Chem. Phys. 9, 4575-4591. DOI: 10.5194/acp-9-4575-2009.

Reid, J.S., Eck, T.F., Christopher, S.A., Koppmann, R., Dubovik, O., Eleuterio, D.P., Holben, B.N., Reid, E.A., Zhang, J., 2005. A review of biomass burning emissions part III: intensive optical properties of biomass burning particles. Atmos. Chem. Phys. 5, 827-849. DOI: 10.5194/acp-5-827-2005.

Rivera, H., Ogren, J.A., Andrews, E., Mayol-Bracero, O.L., 2017. Variations in the physicochemical and optical properties of natural aerosols in Puerto Rico – Implications for climate. Atmos. Chem. Phys. Discuss. DOI: 10.5194/acp-2017-703.

Rizzo, L.V., Correia, A.L., Artaxo, P., Procópio, A.S., Andreae, M.O., 2011. Spectral dependence of aerosol light absorption over the Amazon Basin. Atmos. Chem. Phys. 11, 8899-8912. DOI: 10.5194/acp-11-8899-2011.

Romano, S., Perrone, M.R., Pavese, G., Esposito, F., Calvello, M., 2019a. Optical properties of PM2.5 particles: results from a monitoring campaign in southeastern Italy. Atmos. Environ. 203, 35-47. DOI: 10.1016/j.atmosenv.2019.01.037.

Romano, S., Di Salvo, M., Rispoli, G., Alifano, P., Perrone, M.R., Talà, A., 2019b. Airborne Bacteria in the Central Mediterranean: Structure and role of meteorology and air mass transport. Sci. Total. Environ. 697, 134020. DOI: 10.1016/j.scitotenv.2019.134020.

Russell, P.B., Kacenelenbogen, M., Livingston, J.M., Hasekamp, O.P., Burton, S.P., Schuster, G.L., Johnson, M.S., Knobelspiesse, K.D., Redemann, J., Ramachandran, S., Holben, B., 2014. A Multi-parameter aerosol classification method and its application to retrievals from spaceborne polarimetry. J. Geophys. Res. Atmos. 119, 9838-9863. DOI: 10.1002/2013JD021411.

Schmeisser, L., Andrews, E., Ogren, J.A., Sheridan, P., Jefferson, A., Sharma, S., Kim, J.E., Sherman, J.P., Sorribas, M., Kalapov, I., Arsov, T., Angelov, C., Mayol-Bracero, O.L., Labuschagne, C., Kim, S.-W., Hoffer, A., Lin, N.-H., Chia, H.-P., Bergin, M., Sun, J., Liu, P., Wu, H., 2017. Classifying aerosol type using in situ surface spectral aerosol optical properties. Atmos. Chem. Phys. 17, 12097-12120. DOI: 10.5194/acp-17-12097-2017.

Schuster, G.L., Dubovik, O., Holben, B.N., 2006. Ångström exponent and bimodal aerosol size distributions. J. Geophys. Res. 111, D07207. DOI: 10.1029/2005JD006328.

Seinfeld, J.H., 1986. Atmospheric Chemistry and Physics of Air Pollution. John Willey, New York.

Seinfeld, J.H., Pandis, S.N., 1998. Atmospheric Chemistry and Physics: From Air Pollution to Climate Change. J. Wiley &Sons, INC.

Singh, R.P., Dey, S., Tripathi, S.N., Tare, V., Holben, B., 2004. Variability of aerosol parameters over Kanpur, northern India. J. Geophys. Res. 109, D23. DOI: 10.1029/2004JD004966.

Tafuro, A.M., Kinne, S., De Tomasi, F., Perrone, M.R., 2007. Annual cycle of aerosol direct radiative effect over southeast Italy and sensitivity studies. J. Geophys. Res. 112, D20202. DOI: 10.1029/2006JD008265.

Ten Brink, H.M., Veefkind, J.P., Waijers-IJpelaan, A., van der Hage, J.C.H., 1996. Aerosol light-scattering in The Netherlands. Atmos. Environ. 30, 4251-4261. DOI: 10.1016/1352-2310(96) 00091-X.

Titos, G., Foyo-Moreno, I., Lyamani, H., Querol, X., Alastuey, A., Alados-Arboledas, L., 2012. Optical properties and chemical composition of aerosol particles at an urban location: An estimation of the aerosol mass scattering and absorption efficiencies. J. Geophys. Res. 117, D04206. DOI: 10.1029/2011JD016671.

Vecchi, R., Chiari, M., D'Alessandro, A., Fermo, P., Lucarelli, F., Mazzei, F., Nava, S., Piazzalunga, A., Prati, P., Silvani, F., Valli, G., 2008. A mass closure and PMF source apportionment study on the sub-micron sized aerosol fraction at urban sites in Italy. Atmos. Environ. 42, 2240-2253. DOI: 10.1016/j.atmosenv.2007.11.039.

Viana M., Kuhlbusch, T.A.J., Querol, X., Alastuey, A., Harrison, R.M., Hopke, P.K., Winiwarter, W., Vallius, M., Szidat, S., Prévôt, A.S.H., Hueglin, C., Bloemen, H., Wåhlin, P., Vecchi, R., Miranda, A.I., Kasper-Giebl, A., Maenhaut, W., Hitzenberger, R., 2008. Source apportionment of PM in Europe: a review of methods and results. J. Aerosol Sci. 39, 827-849. DOI: 10.1016/ j.jaerosci.2008.05.007.

Wang, Y.H., Liu, Z.R., Zhang, J.K., Hu, B., Ji, D.S., Yu, Y.C., Wang, Y.S., 2015. Aerosol physicochemical properties and implications for visibility during an intense haze episode during winter in Beijing. Atmos. Chem. Phys. 15, 3205-3215. DOI: 10.5194/acp-15-3205-2015.

Wiscombe, W.J., Grams, G.W., 1976. The backscattered fraction in two-stream approximations. J. Atmos. Sci. 33, 2440-2451. DOI: 10.1175/1520-0469(1976)033<2440:TBFITS>2.0.CO;2.

Yang, M., Howell, S.G., Zhuang, J., Huebert, B.J., 2009. Attribution of aerosol light absorption to black carbon, brown carbon, and dust in China – interpretations of atmospheric measurements during EAST-AIRE. Atmos. Chem. Phys. 9, 2035-2050. DOI: 10.5194/acp-9-2035-2009.

Yu, H., Kaufman, Y. J., Chin, M., Feingold, G., Remer, L.A., Anderson, T.L., Balkanski, Y., Bellouin, N., Boucher, O., Christopher, S., DeCola, P., Kahn, R., Koch, D., Loeb, N., Reddy, M.S.,

Schulz, M., Takemura, T., Zhou, M., 2006. A review of measurement-based assessments of the aerosol direct radiative effect and forcing. Atmos. Chem. Phys. 6, 613-666. DOI: 10.5194/acp-6-613-2006.

Yu, X., Shen, L., Xiao, S., Ma, J., Lü, R., Zhu, B., Hu, J., Chen, K., Zhu, J., 2019. Chemical and Optical Properties of Atmospheric Aerosols during the Polluted Periods in a Megacity in the Yangtze River Delta, China. Aerosol Air Qual. Res. 19, 103-117. DOI: 10.4209/aaqr.2017.12.0572.

Yubero, E., Galindo, N., Nicolás, J.F., Crespo, J., Calzolai, G., Lucarelli, F., 2015. Temporal variations of $PM_1$ major components in an urban street canyon. Environ. Sci. Pollut. Res. 22, 13328-13335. DOI: 10.1007/s11356-015-4599-z.

Zhang, X.Y., Wang, Y.Q., Niu, T., Zhang, X.C., Gong, S.L., Zhang, Y.M., Sun, J.Y., 2012. Atmospheric aerosol compositions in China: spatial/temporal variability, chemical signature, regional haze distribution and comparisons with global aerosols. Atmos. Chem. Phys. 12, 779-799. DOI: 10.5194/acp-12-779-2012.

**Table 1.** Mean mass concentrations (in ng $m^{-3}$) and related standard errors of the mean (SEMs) of the analyzed components in 82 PM10 samples for the whole analyzed period (from November 2011 to November 2012), Autumn-Winter (AW, October–March), and Spring-Summer (SS, April–September). The mean mass percentages of the measured species with respect to the total sampled mass are reported in brackets. The PM10 mass concentration and the PM1/PM10 ratio have been also reported.

| Species | Yearly mean | SEM | AW mean | SEM | SS mean | SEM |
|---|---|---|---|---|---|---|
| $Na^+$ | 570 (1.5) | 57 | 552 (1.3) | 69 | 585 (1.6) | 88 |
| $NH_4^+$ | 1403 (3.6) | 79 | 1350 (3.3) | 148 | 1447 (4.0) | 78 |
| $K^+$ | 508 (1.3) | 54 | 538 (1.3) | 98 | 483 (1.3) | 56 |
| $Mg^{2+}$ | 191 (0.5) | 9 | 180 (0.4) | 12 | 201 (0.6) | 13 |
| $Ca^{2+}$ | 1337 (3.5) | 90 | 810 (2.0) | 88 | 1771 (4.9) | 113 |
| $Cl^-$ | 609 (1.6) | 74 | 643 (1.6) | 77 | 581 (1.6) | 121 |
| $NO_3^-$ | 1532 (4.0) | 163 | 2072 (5.0) | 330 | 1088 (3.0) | 81 |
| $SO_4^{2-}$ | 3410 (8.8) | 167 | 2962 (7.2) | 248 | 3778 (10.4) | 212 |
| Al | 395 (1.0) | 31 | 242 (0.6) | 28 | 521 (1.4) | 44 |
| Cr | 3.1 (0.01) | 0.2 | 2.0 (0.005) | 0.2 | 4.0 (0.01) | 0.3 |
| Cu | 17 (0.04) | 2 | 18 (0.04) | 4 | 17 (0.05) | 2 |
| Fe | 395 (1.0) | 27 | 277 (0.7) | 35 | 493 (1.4) | 33 |
| Mn | 10.4 (0.03) | 0.7 | 6.9 (0.02) | 0.9 | 13.3 (0.04) | 0.9 |
| V | 3.9 (0.01) | 0.3 | 2.7 (0.007) | 0.4 | 4.9 (0.01) | 0.3 |
| Ti | 26 (0.07) | 2 | 14 (0.03) | 2 | 36 (0.1) | 3 |
| Zn | 23 (0.06) | 2 | 26 (0.06) | 3 | 20 (0.05) | 2 |
| OC | 10920 (28) | 700 | 11400 (28) | 1250 | 10520 (29) | 770 |
| EC | 3160 (8.2) | 225 | 3480 (8.4) | 370 | 2900 (7.9) | 270 |
| PM10 | 38600 | 1300 | 41200 | 2500 | 36500 | 1200 |
| PM1/PM10 | 0.39 | 0.01 | 0.41 | 0.02 | 0.38 | 0.01 |

**Table 2.** Mean value and related standard error of the mean (SEM) of the optical parameters (scattering coefficient $\sigma_s$, scattering coefficient difference $\Delta\sigma_s$, backscattering coefficient $\beta_s$, backscattering coefficient difference $\Delta\beta_s$, Ångström exponent $\mathring{A}$, Ångström exponent difference $\Delta\mathring{A}$, asymmetry parameter $g$, and PM10 mass scattering efficiency $\Sigma_{PM10}$) calculated from nephelometer measurements for the whole analyzed period (from November 2011 to November 2012), Autumn-Winter (AW, from October to March), and Spring-Summer (SS, from April to September).

| Parameters | λ (nm) | Yearly mean | SEM | AW mean | SEM | SS mean | SEM |
|---|---|---|---|---|---|---|---|
| $\sigma_s$ ($Mm^{-1}$) | 450 | 129 | 8 | 163 | 16 | 102 | 5 |
| $\sigma_s$ ($Mm^{-1}$) | 525 | 104 | 7 | 130 | 13 | 82 | 4 |
| $\sigma_s$ ($Mm^{-1}$) | 635 | 83 | 5 | 100 | 10 | 68 | 3 |
| $\Delta\sigma_s$ (%) | | 34.9 | 0.5 | 36.9 | 0.6 | 33.3 | 0.7 |
| $\beta_s$ ($Mm^{-1}$) | 450 | 16 | 2 | 20 | 3 | 13 | 1 |
| $\beta_s$ ($Mm^{-1}$) | 525 | 14 | 1 | 17 | 2 | 12 | 1 |
| $\beta_s$ ($Mm^{-1}$) | 635 | 12 | 1 | 15 | 1 | 10 | 1 |
| $\Delta\beta_s$ (%) | | 21.5 | 0.9 | 22.0 | 1.7 | 21.1 | 0.8 |
| $\mathring{A}$ | 450-635 | 1.2 | 0.1 | 1.3 | 0.1 | 1.1 | 0.1 |
| $\Delta\mathring{A}$ | 450-635 | 0.26 | 0.03 | 0.15 | 0.03 | 0.35 | 0.03 |
| $g$ | 450 | 0.59 | 0.01 | 0.59 | 0.01 | 0.58 | 0.01 |
| $g$ | 525 | 0.56 | 0.01 | 0.56 | 0.01 | 0.55 | 0.01 |
| $g$ | 635 | 0.53 | 0.01 | 0.52 | 0.01 | 0.53 | 0.01 |
| $\Sigma_{PM10}$ ($m^2g^{-1}$) | 450 | 4.9 | 0.5 | 5.4 | 0.6 | 2.0 | 0.5 |
| $\Sigma_{PM10}$ ($m^2g^{-1}$) | 525 | 3.9 | 0.4 | 4.3 | 0.5 | 1.6 | 0.4 |
| $\Sigma_{PM10}$ ($m^2g^{-1}$) | 635 | 3.0 | 0.3 | 3.3 | 0.4 | 1.4 | 0.3 |

**Table 3.** Mean values and related standard errors of the mean (SEM) of the PM10 mass concentration and the extensive optical parameters (scattering coefficient $\sigma_s$ and backscattering coefficient $\beta_s$) associated with the Traffic (TRA), Biomass Burning + Nitrates (BBN), Soil Dust (SDU), ammonium Sulphate (SUL), and Aged Sea-salt (ASS) pollution sources by the Positive Matrix Factorization (PMF) technique. Intensive optical parameter values (scattering coefficient difference $\Delta\sigma_s$, backscattering coefficient difference $\Delta\beta_s$, Ångström exponent $\mathring{A}$, Ångström exponent difference $\Delta\mathring{A}$, asymmetry parameter $g$, and PM10 mass scattering efficiency $\Sigma_{PM10}$) associated with the identified pollution sources are also reported.

| Parameters | λ (nm) | TRA | | BBN | | SDU | | SUL | | ASS | |
|---|---|---|---|---|---|---|---|---|---|---|---|
| | | mean | SEM | mean | SEM | mean | SEM | mean | SEM | mean | SEM |
| PM10 (μg m$^{-3}$) | | 10.5 | 1.0 | 10.2 | 1.2 | 5.5 | 0.5 | 6.3 | 0.5 | 4.7 | 0.6 |
| $\sigma_s$ (Mm$^{-1}$) | 450 | 36 | 3 | 51 | 6 | 0 | 0 | 32 | 2 | 2.9 | 0.4 |
| $\sigma_s$ (Mm$^{-1}$) | 525 | 30 | 3 | 40 | 5 | 0 | 0 | 25 | 2 | 3.2 | 0.4 |
| $\sigma_s$ (Mm$^{-1}$) | 635 | 26 | 2 | 30 | 4 | 0 | 0 | 19 | 1 | 3.6 | 0.5 |
| $\Delta\sigma_s$ (%) | | 28 | | 42 | | | | 41 | | -25 | |
| $\beta_s$ (Mm$^{-1}$) | 450 | 4.9 | 0.5 | 6.8 | 0.8 | 0.16 | 0.01 | 3.1 | 0.2 | 0.8 | 0.1 |
| $\beta_s$ (Mm$^{-1}$) | 525 | 4.2 | 0.4 | 5.7 | 0.7 | 0.25 | 0.02 | 2.8 | 0.2 | 0.8 | 0.1 |
| $\beta_s$ (Mm$^{-1}$) | 635 | 3.5 | 0.3 | 4.6 | 0.6 | 0.26 | 0.02 | 2.7 | 0.2 | 0.9 | 0.1 |
| $\Delta\beta_s$ (%) | | 29 | | 32 | | -61 | | 11 | | -23 | |
| $\mathring{A}$ | 450-635 | 0.96 | | 1.57 | | | | 1.54 | | -0.65 | |
| $\Delta\mathring{A}$ | 450-635 | 0.54 | | -0.06 | | | | 0.24 | | 0.12 | |
| $g$ | 450 | 0.57 | | 0.58 | | | | 0.67 | | 0.33 | |
| $g$ | 525 | 0.56 | | 0.56 | | | | 0.62 | | 0.35 | |
| $g$ | 635 | 0.57 | | 0.53 | | | | 0.55 | | 0.34 | |
| $\Sigma_{PM10}$ (m$^2$ g$^{-1}$) | 450 | 3.4 | | 5.0 | | | | 5.0 | | 0.6 | |
| $\Sigma_{PM10}$ (m$^2$ g$^{-1}$) | 525 | 2.8 | | 4.0 | | | | 3.9 | | 0.7 | |
| $\Sigma_{PM10}$ (m$^2$ g$^{-1}$) | 635 | 2.4 | | 2.9 | | | | 3.0 | | 0.8 | |

**Table 4.** Comparison between the values of intensive aerosol optical parameters (scattering Ångström exponent *Å*, asymmetry parameter *g*, and mass scattering efficiency $\Sigma_{PM}$) of this study for the sources identified by PMF (biomass burning and nitrate BBN, ammonium sulphate SUL, traffic TRA, and aged sea salt ASS) and the ones reported in different studies from surface in situ measurements.

| Source | Parameters | λ (nm) | Values | Period | Site | Reference |
|---|---|---|---|---|---|---|
| **BBN** | ***Å*** | 450-635 | **1.57** | Nov. 2011 – Nov. 2012 | Lecce (Italy) | **This study** |
| | | 450-550 | > 1.3 | Dec. 1995 – Mar. 2006 | from different Pacific sites | Clarke and Kapustin (2010) |
| | | 450-550 | > 1.5 | Jun. 2010 | Sacramento (USA) | Cappa et al. (2016) |
| | | 467-660 | > 1.5 | Oct. 2010 – Mar. 2012 | Rome (Italy) | Costabile et al. (2013) |
| | | 450-700 | 1.52±0.18 | Mar. 2005 | Beijing (China) | Yang et al. (2009) |
| | | 450-635 | 1.8±0.3 | Jan. 2012 – Dec. 2015 | Chacaltaya (Bolivia) | Aurélien et al. (2019) |
| | | 450-700 | 0.8 – 1.5 | May. 2009 – Nov. 2009 | Gosan (South Korea) | Lee et al. (2012) |
| | ***g*** | 525 | **0.56** | Nov. 2011 – Nov. 2012 | Lecce (Italy) | **This study** |
| | | 550 | 0.55 – 0.65 | Jan. 1993 – Dec. 2000 | from different worldwide sites | Reid et al. (2005) |
| | | 550 | 0.40 – 0.71 | Aug. 2001 – Sep. 2001 | Leon (Spain) | Alonso-Blanco et al. (2014) |
| | $\Sigma_{PM}$ | 525 | **4.0** | Nov. 2011 – Nov. 2012 | Lecce (Italy) | **This study** |
| | | 550 | 3.6 – 4.3 | Jan. 1993 – Dec. 2000 | from different worldwide sites | Reid et al. (2005) |
| | | 530 | 5.5±0.5 | Jul. 2002 – Sep. 2002 | Yosemite Park (USA) | McMeeking et al. (2005) |
| **SUL** | ***Å*** | 450-635 | **1.54** | Nov. 2011 – Nov. 2012 | Lecce (Italy) | **This study** |
| | | 450-650 | 1.77 | - | from different worldwide sites | D'Almeida et al. (1991) |
| | ***g*** | 525 | **0.62** | Nov. 2011 – Nov. 2012 | Lecce (Italy) | **This study** |
| | | 550 | 0.72 | - | from different worldwide sites | D'Almeida |
| | | 550 | 0.64 | May 2007 | Toulon (France) | Mallet et al. (2011) |
| | $\Sigma_{PM}$ | 525 | **3.9** | Nov. 2011 – Nov. 2012 | Lecce (Italy) | **This study** |
| | | 525 | 2.5±0.6 | Jan. 1989 – Dec. 2003 | from different worldwide sites | Hand and Malm (2007) |
| | | 550 | 3.7±0.1 | Jul. 1995 | Tenerife (Spain) | Maring et al. (2000) |
| **TRA** | ***Å*** | 450-635 | **0.96** | Nov. 2011 – Nov. 2012 | Lecce (Italy) | **This study** |
| | | 450-700 | 0.96 | Jan. 2012 – Dec. 2013 | from different worldwide sites | Schmeisser et al. (2017) |
| | | 450-550 | < 1.5 | Jun. 2010 | Sacramento (USA) | Cappa et al. (2016) |
| | | 450-700 | 1.39±0.20 | Mar. 2005 | Beijing (China) | Yang et al. (2009) |
| | | 450-700 | 1.4 – 1.8 | May. 2009 – Nov. 2009 | Gosan (South Korea) | Lee et al. (2012) |
| | | 450-700 | 0.99 | Jan. 2015 | Nanjing (China) | Yu et al. (2019) |
| | ***g*** | 525 | **0.56** | Nov. 2011 – Nov. 2012 | Lecce (Italy) | **This study** |
| | | 550 | 0.68±0.02 | Jan. 2015 | Nanjing (China) | Yu et al. (2019) |
| | $\Sigma_{PM}$ | 525 | **2.8** | Nov. 2011 – Nov. 2012 | Lecce (Italy) | **This study** |
| | | 550 | 1.40 – 5.36 | Jan. 2015 | Nanjing (China) | Yu et al. (2019) |
| **ASS** | ***Å*** | 450-635 | **-0.65** | Nov. 2011 – Nov. 2012 | Lecce (Italy) | **This study** |
| | | 450-635 | -0.35 – -0.09 | Feb. 2016 – Mar. 2016 | Lecce (Italy) | Romano et al. (2019a) |
| | | 467-660 | < 0.5 | Oct. 2010 – Mar. 2012 | Rome (Italy) | Costabile et al. (2013) |
| | | 450-700 | 0.33±0.18 | Jan. 2005 – Dec. 2010 | San Juan (Puerto Rico) | Rivera et al. (2017) |
| | ***g*** | **525** | **0.35** | Nov. 2011 – Nov. 2012 | Lecce (Italy) | **This study** |
| | | 532 | 0.56±0.05 | Jun. 2016 | Granada (Spain) | Horvath et al. (2018) |
| | | 550 | 0.65 | May 2002 – Dec. 2004 | Trinidad Head (USA) | Fiebig and Ogren (2006) |
| | $\Sigma_{PM}$ | **525** | **0.7** | Nov. 2011 – Nov. 2012 | Lecce (Italy) | **This study** |
| | | 670 | 0.52 | Dec. 1994 – Feb. 1995 | Sal Island (Cape Verde) | Chiapello et al. (1999) |
| | | 550 | 0.33 | - | from different worldwide sites | D'Almeida et al. (1991) |
| | | 530 | 0.3 – 0.5 | Apr. 1994 – May 1994 | Barbados | Li et al. (1996) |
| | | 550 | 2.2±0.5 | Dec. 1991 – Mar. 2001 | from different worldwide sites | Hand and Malm (2007) |

**Table 5.** Comparison between experimental and PMF (Positive Matrix Factorization)-estimated total values of PM10 concentrations and optical parameters (scattering coefficient $\sigma_s$, backscattering coefficient $\beta_s$, Ångström exponent $Å$, Ångström exponent difference $\Delta Å$, and asymmetry parameter $g$) for three case studies. PM10 concentrations and optical parameter values estimated by PMF for the Traffic (TRA), Biomass Burning + Nitrates (BBN), Soil Dust (SDU), ammonium Sulphate (SUL), and Aged Sea-salt (ASS) pollution sources are also reported. Values related to the prevailing pollution source, according to the PM10 mass reconstruction, have been reported in bold.

| Case Study | Parameters | λ (nm) | experimental | PMF | | | | | |
|---|---|---|---|---|---|---|---|---|---|
| | | | | total | TRA | BBN | SDU | SUL | ASS |
| December 1, 2011 | PM10 (μg m$^{-3}$) | | 53±3 | 63.6 | 4.3 | **49.2** | 1.3 | 7.7 | 1.1 |
| | $\sigma_s$ (Mm$^{-1}$) | 450 | 336±11 | 302 | 15 | **247** | 0 | 39 | 1 |
| | $\beta_s$ (Mm$^{-1}$) | 450 | 36.3±1.2 | 38.8 | 2.0 | **32.7** | 0.1 | 3.8 | 0.2 |
| | $Å$ | 450-635 | 1.51±0.01 | 1.53 | 0.96 | **1.57** | | 1.54 | -0.06 |
| | $\Delta Å$ | 450-635 | -0.10±0.01 | 0.01 | 0.54 | **-0.06** | | 0.24 | 0.12 |
| | $g$ | 450 | 0.64±0.02 | 0.59 | 0.57 | **0.58** | | 0.67 | 0.33 |
| August 31, 2012 | PM10 (μg m$^{-3}$) | | 40±2 | 39.8 | **26.6** | 2.1 | 5.2 | 4.7 | 1.2 |
| | $\sigma_s$ (Mm$^{-1}$) | 450 | 109±7 | 126 | **90** | 11 | 0 | 24 | 1 |
| | $\beta_s$ (Mm$^{-1}$) | 450 | 16.0±1.1 | 16.5 | **12.5** | 1.4 | 0.1 | 2.3 | 0.2 |
| | $Å$ | 450-635 | 1.02±0.01 | 1.09 | **0.96** | 1.57 | | 1.54 | -0.06 |
| | $\Delta Å$ | 450-635 | 0.69±0.01 | 0.45 | **0.54** | -0.06 | | 0.24 | 0.12 |
| | $g$ | 450 | 0.60±0.02 | 0.58 | **0.57** | 0.58 | | 0.67 | 0.33 |
| April 5, 2012 | PM10 (μg m$^{-3}$) | | 43±2 | 52.7 | 0.0 | 7.3 | 9.7 | 0.0 | **35.6** |
| | $\sigma_s$ (Mm$^{-1}$) | 450 | 104±5 | 59 | 0 | 37 | 0 | 0 | **22** |
| | $\beta_s$ (Mm$^{-1}$) | 450 | 12.6±1.0 | 11.0 | 0.0 | 4.9 | 0.3 | 0.0 | **5.8** |
| | $Å$ | 450-635 | 0.49±0.01 | 0.54 | 0.96 | 1.57 | | 1.54 | **-0.06** |
| | $\Delta Å$ | 450-635 | 0.37±0.01 | 0.23 | 0.54 | -0.06 | | 0.24 | **0.12** |
| | $g$ | 450 | 0.61±0.02 | 0.47 | 0.57 | 0.58 | | 0.67 | **0.33** |

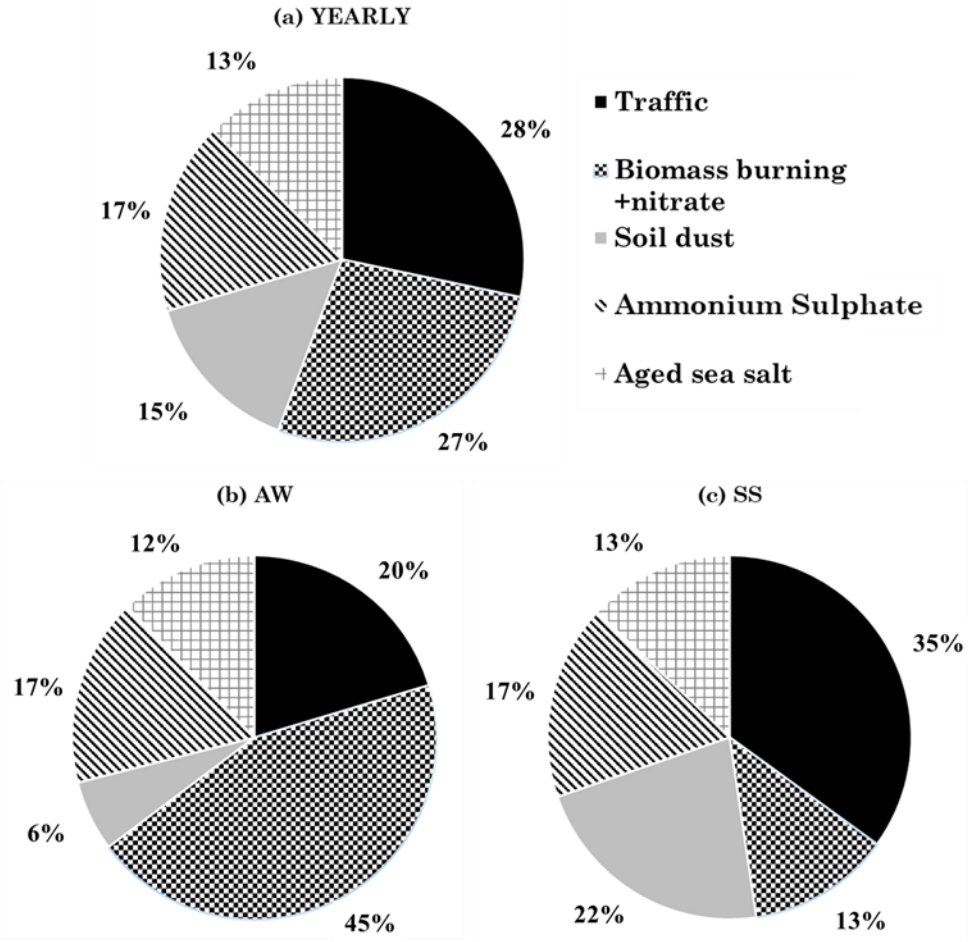


**Figure 1.** Mean percentage contribution of the PM10 mass associated with the pollution sources (Traffic, Biomass Burning+Nitrates, Soil Dust, ammonium Sulphate, and Aged Sea-salt) identified by the Positive Matrix Factorization (PMF) technique for (a) the whole analyzed period (from November 2011 to November 2012), (b) Autumn-Winter (AW, October–March), and (c) Spring-Summer (SS, April–September).

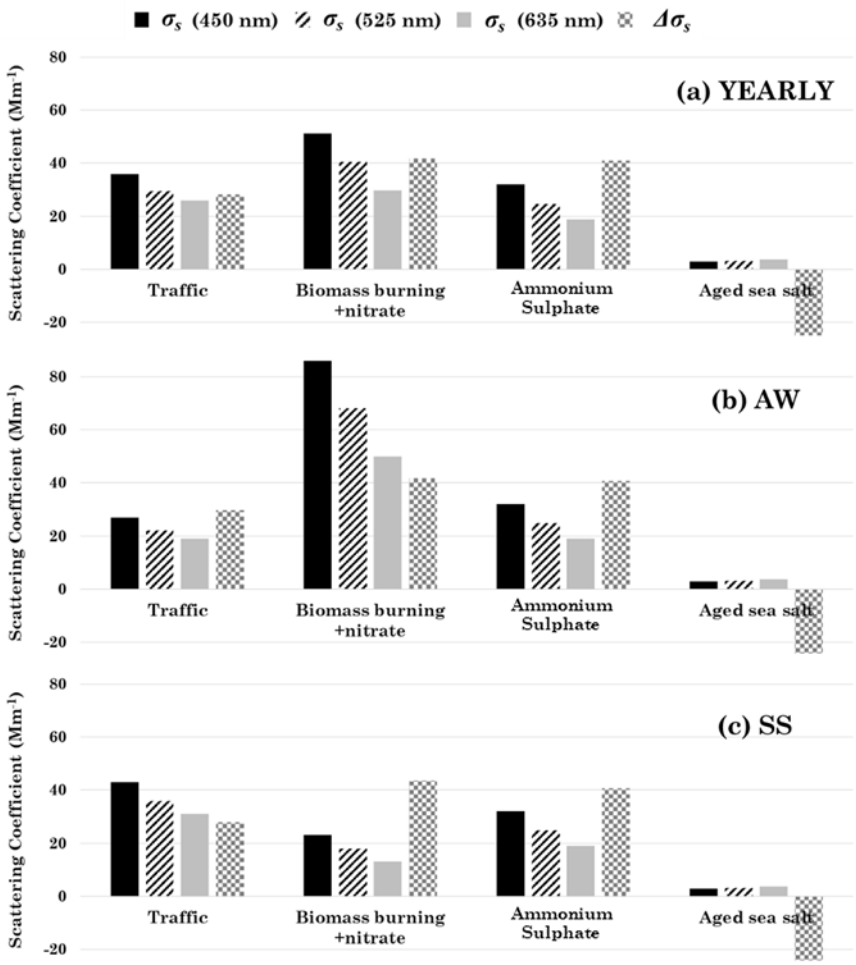


**Figure 2.** Bar chart of the mean values of the aerosol scattering coefficient ($\sigma_s$) at 450, 525, and 635 nm and the related percentage difference ($\Delta\sigma_s$) associated with the pollution sources (Traffic, Biomass Burning+Nitrates, ammonium Sulphate, and Aged Sea-salt) identified by Positive Matrix Factorization (PMF) technique, for (a) the whole analyzed period (from November 2011 to November 2012), (b) Autumn-Winter (AW, October–March), and (c) Spring-Summer (SS, April–September).

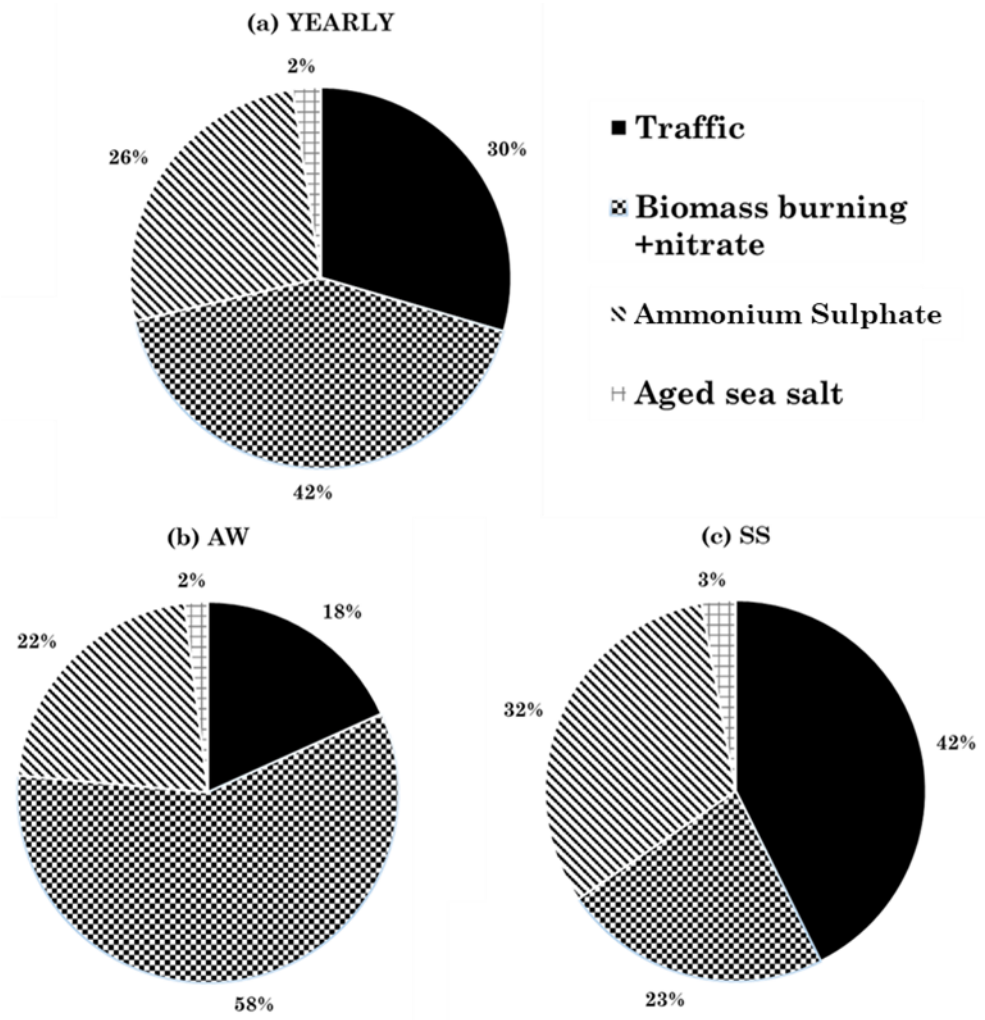


**Figure 3.** Mean percentage contribution of the scattering coefficient at 450 nm associated with the pollution sources (Traffic, Biomass Burning+Nitrates, ammonium Sulphate, and Aged Sea-salt) identified by the Positive Matrix Factorization (PMF) technique for (a) the whole analyzed period (from November 2011 to November 2012), (b) Autumn-Winter (AW, October–March), and (c) Spring-Summer (SS, April–September).

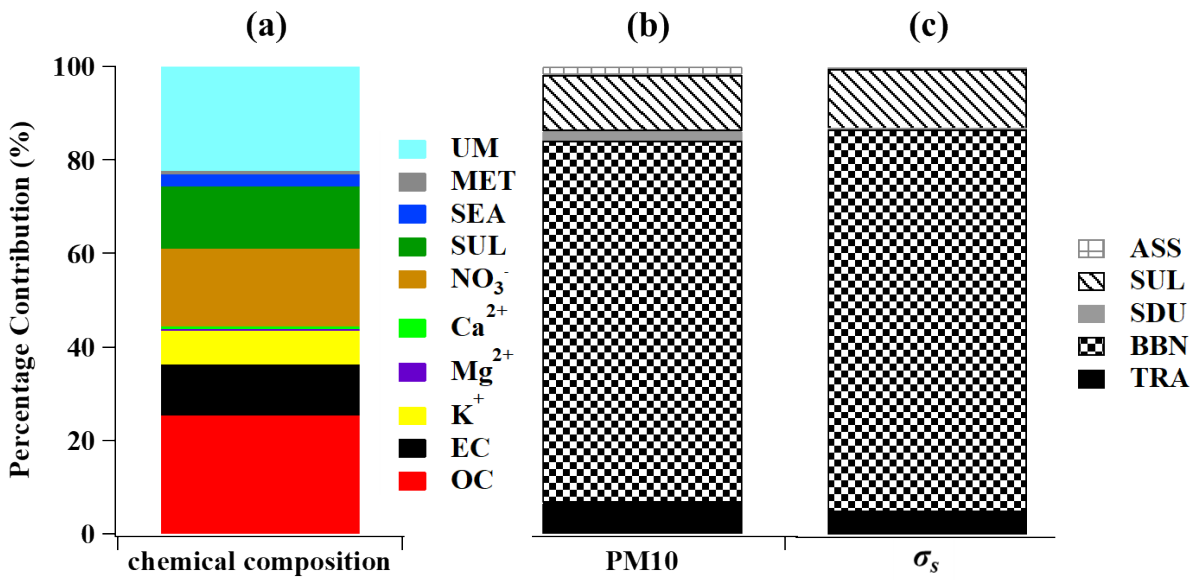


**Figure 4.** Bar plots of (a) the mass percentage contribution of the monitored chemical species, (b) the PM10 and (c) the aerosol scattering coefficient at 450 nm ($\sigma_s$) percentage contributions associated by PMF technique with the identified pollution sources on 1st December 2011. In (a), UM shows the undetermined mass percentage, MET the one due to metals (Al + Cr + Cu + Fe + Mn + Ti), SEA the one due to ($Na^+ + Cl^-$), and SUL the one due to ($SO_4^{2-} + NH_4^+$). In (b) and in (c), Traffic, Biomass Burning + Nitrates, Soil Dust, ammonium Sulphate, and Aged Sea-Salt sources have been denoted as TRA, BBN, SDU, SUL, and ASS, respectively.

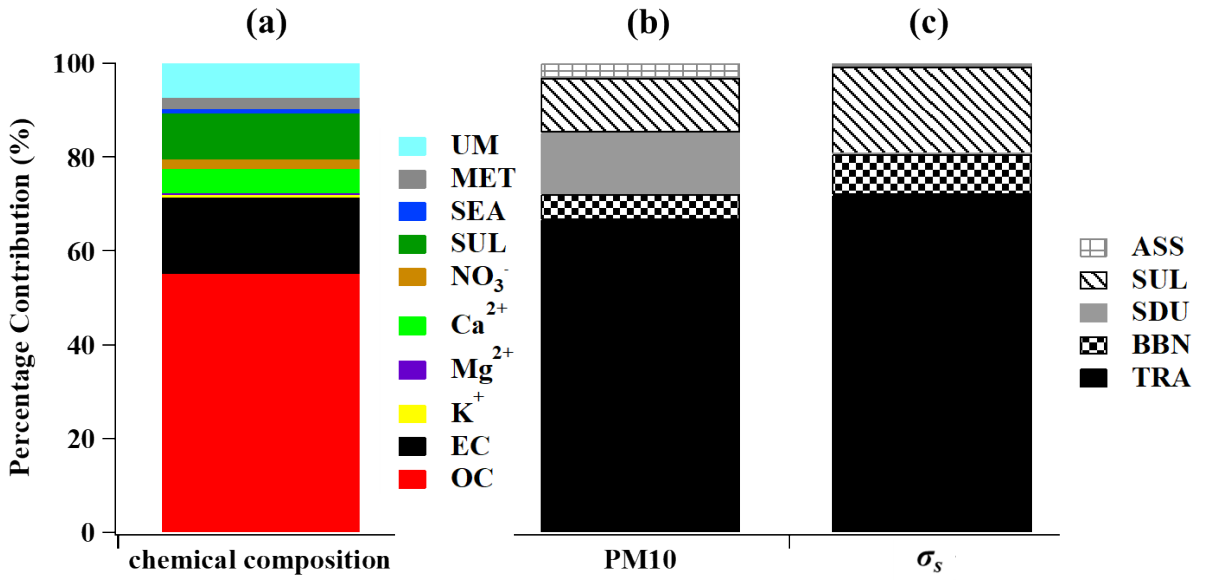


**Figure 5.** Bar plots of (a) the mass percentage contribution of the monitored chemical species, (b) PM10 and (c) aerosol scattering coefficient at 450 nm ($\sigma_s$) percentage contribution associated by PMF technique with the identified pollution sources on 31 August 2012. In (a), UM shows the undetermined mass percentage, MET the one due to metals (Al + Cr + Cu + Fe + Mn + Ti), SEA the one due to ($Na^+ + Cl^-$), and SUL the one due to ($SO_4^{2-} + NH_4^+$). In (b) and in (c), Traffic, Biomass Burning + Nitrates, Soil Dust, ammonium Sulphate, and Aged Sea-Salt sources have been denoted as TRA, BBN, SDU, SUL, and ASS, respectively.

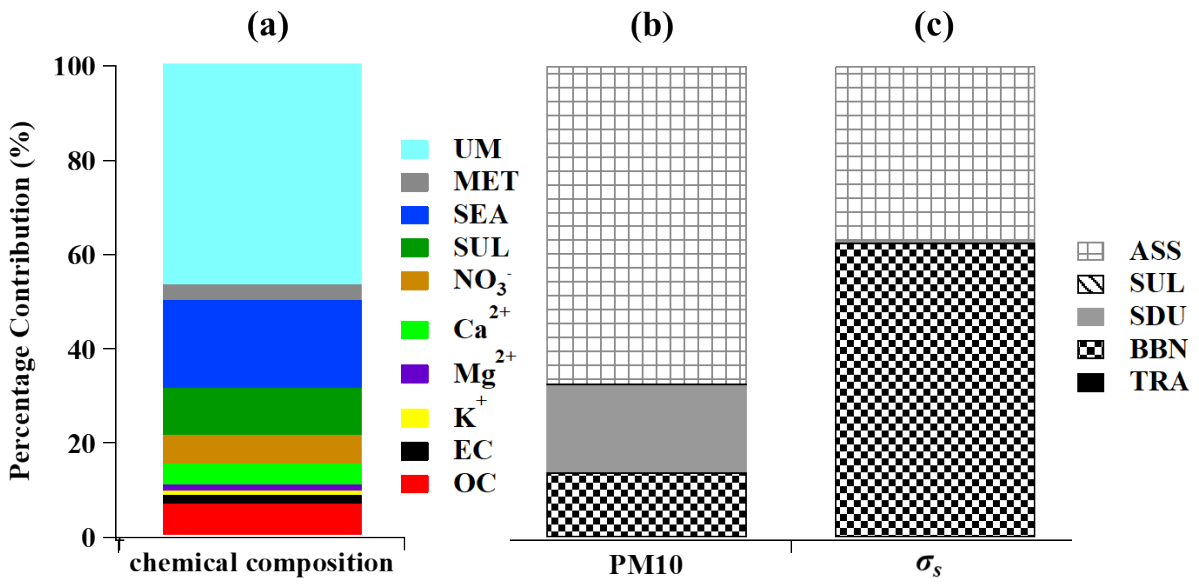


**Figure 6.** Bar plots of (a) the mass percentage contribution of the monitored chemical species, (b) PM10 and (c) aerosol scattering coefficient at 450 nm ($\sigma_s$) percentage contributions associated by PMF technique with the identified pollution sources on 5 April 2012. In (a), UM shows the undetermined mass percentage, MET the one due to metals (Al + Cr + Cu + Fe + Mn + Ti), SEA the one due to ($Na^+ + Cl^-$), and SUL the one due to ($SO_4^{2-} + NH_4^+$). In (b) and in (c), Traffic, Biomass Burning + Nitrates, Soil Dust, ammonium Sulphate, and Aged Sea-Salt sources have been denoted as TRA, BBN, SDU, SUL, and ASS, respectively.

**Declaration of interests**

 The authors declare that they have no known competing financial interests or personal relationships that could have appeared to influence the work reported in this paper.

☐The authors declare the following financial interests/personal relationships which may be considered as potential competing interests:

Salvatore Romano

Roberta Vecchi

Maria Rita Perrone

**Intensive Optical Parameters of Pollution Sources Identified by the Positive Matrix Factorization Technique**

*S. Romano[1], R.Vecchi[2], and M.R. Perrone[1]*

[1]Dipartimento di Matematica e Fisica, Università del Salento, 73100, Lecce (Italy)

[2]Dipartimento di Fisica, Università di Milano, 20133, Milan (Italy)

**Author Contributions**.

Conceptualization: S.R. and M.R.P.

Data curation: S.R. and R.V.

Formal analysis: all authors.

Investigation: S.R. and M.R.P.

Methodology: all authors.

Software: S.R. and R.V.

Supervision: M.R.P.

Writing – review & editing: all authors.

All authors have read and agreed to the submitted version of the manuscript.

# SUPPLEMENTARY MATERIAL

## Intensive Optical Parameters of Pollution Sources identified by the Positive Matrix Factorization Technique

*S. Romano[1], R.Vecchi[2], and M.R. Perrone[1]*

[1]Dipartimento di Matematica e Fisica, Università del Salento, 73100, Lecce (Italy)

[2]Dipartimento di Fisica, Università di Milano, 20133, Milan (Italy)

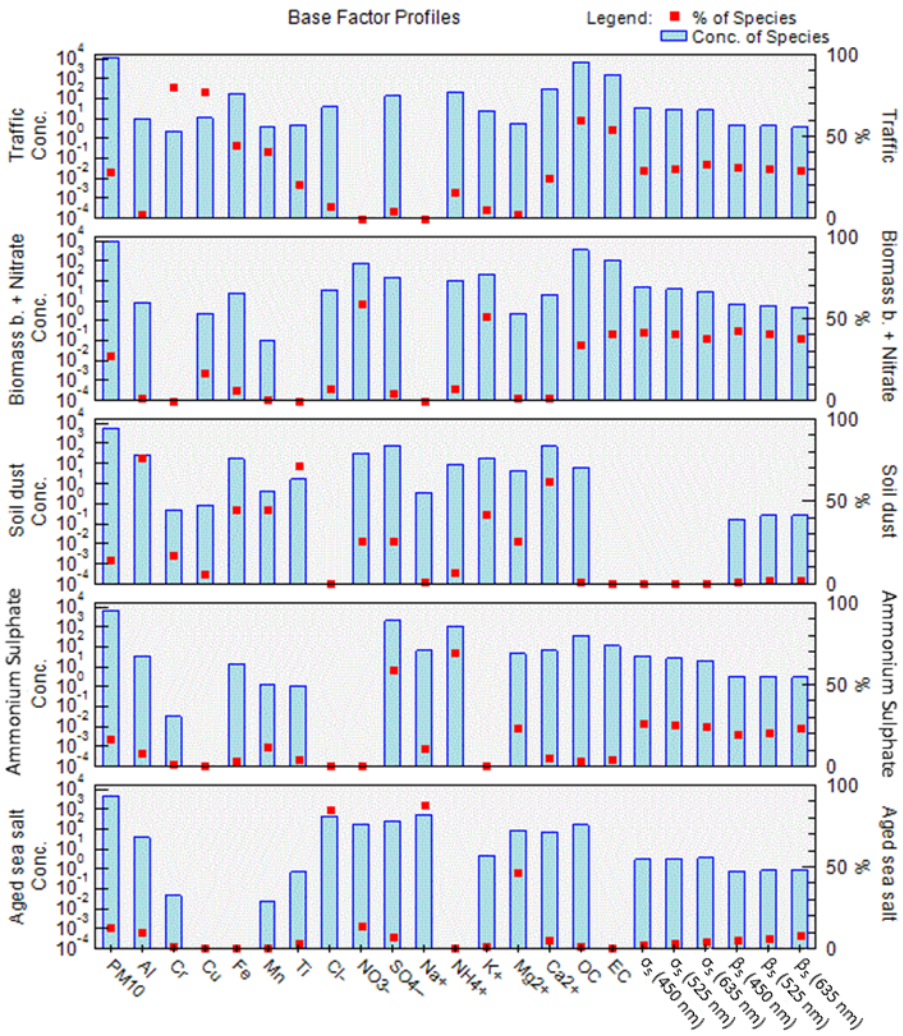


**Figure SM1.** Chemical profiles and percentage contributions of the five pollution sources identified by PMF in the PM10 samples considering the percentage of the chemical species in the factor (as indication of source tracers when higher than 30%), and the scattering $\sigma_s$ and backscattering coefficients $\beta_s$ at 450, 525, 635 nm.

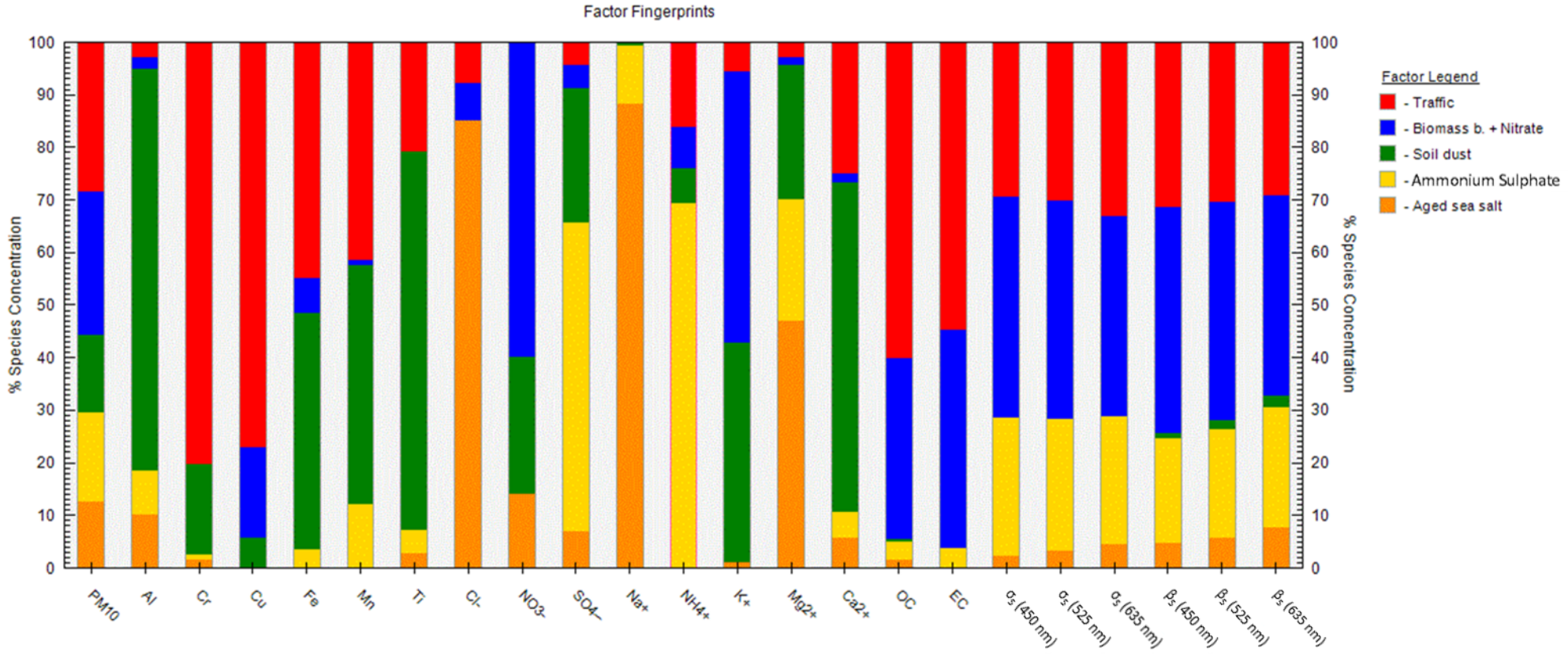


**Figure SM2.** Percentage contributions of chemical components, scattering $\sigma_s$, and backscattering coefficients $\beta_s$ at 450, 525, and 635 nm to the five pollution sources identified by the PMF in PM10 samples.

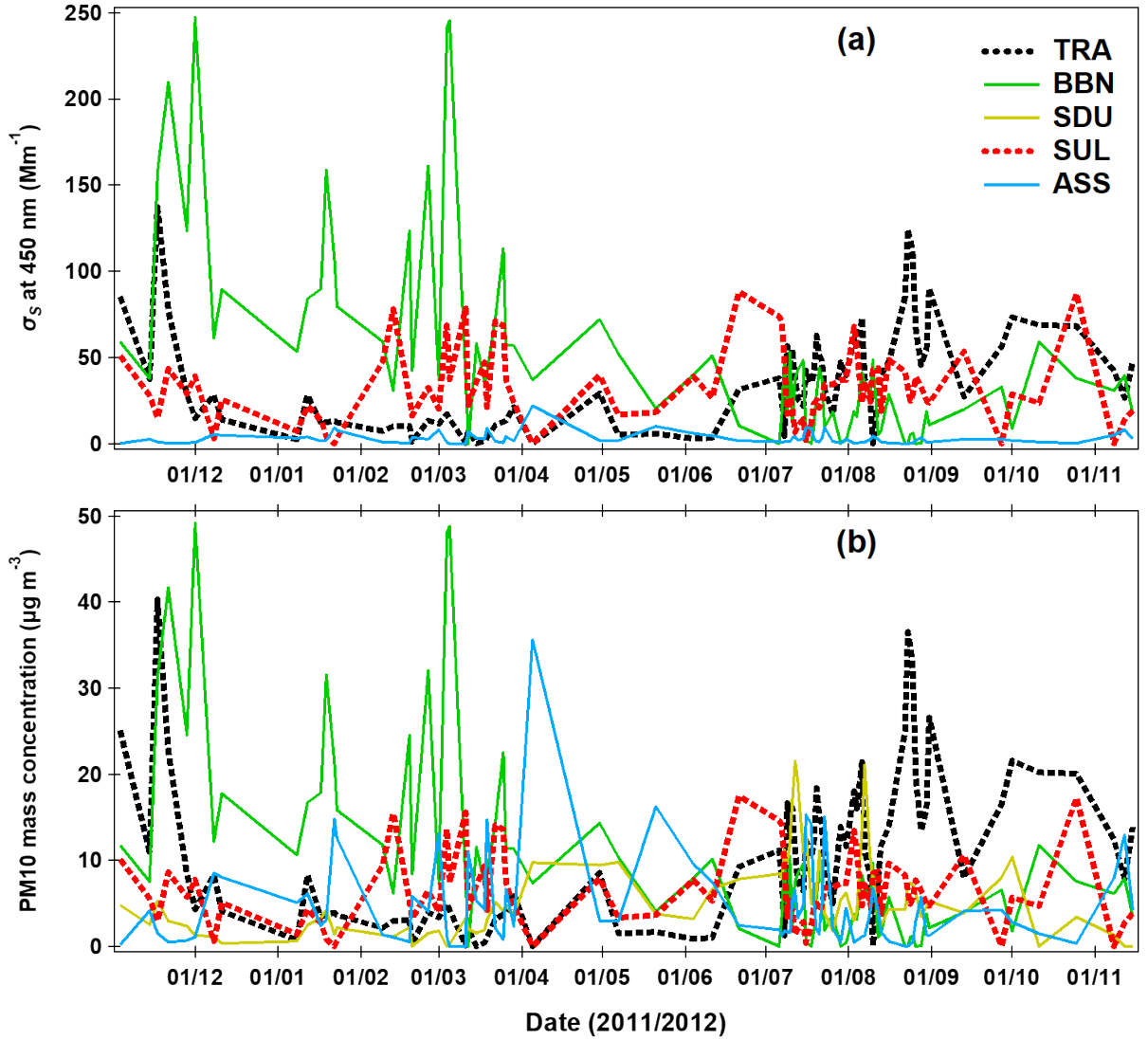


**Figure SM3.** Daily evolution of the identified pollution source (Traffic TRA, Biomass Burning + Nitrates BBN, Soil Dust SDU, Ammonium Sulphate SUL, and Aged Sea-salt ASS) contributions to (a) $\sigma_s$ (at 450 nm) and (b) PM10 mass concentrations.

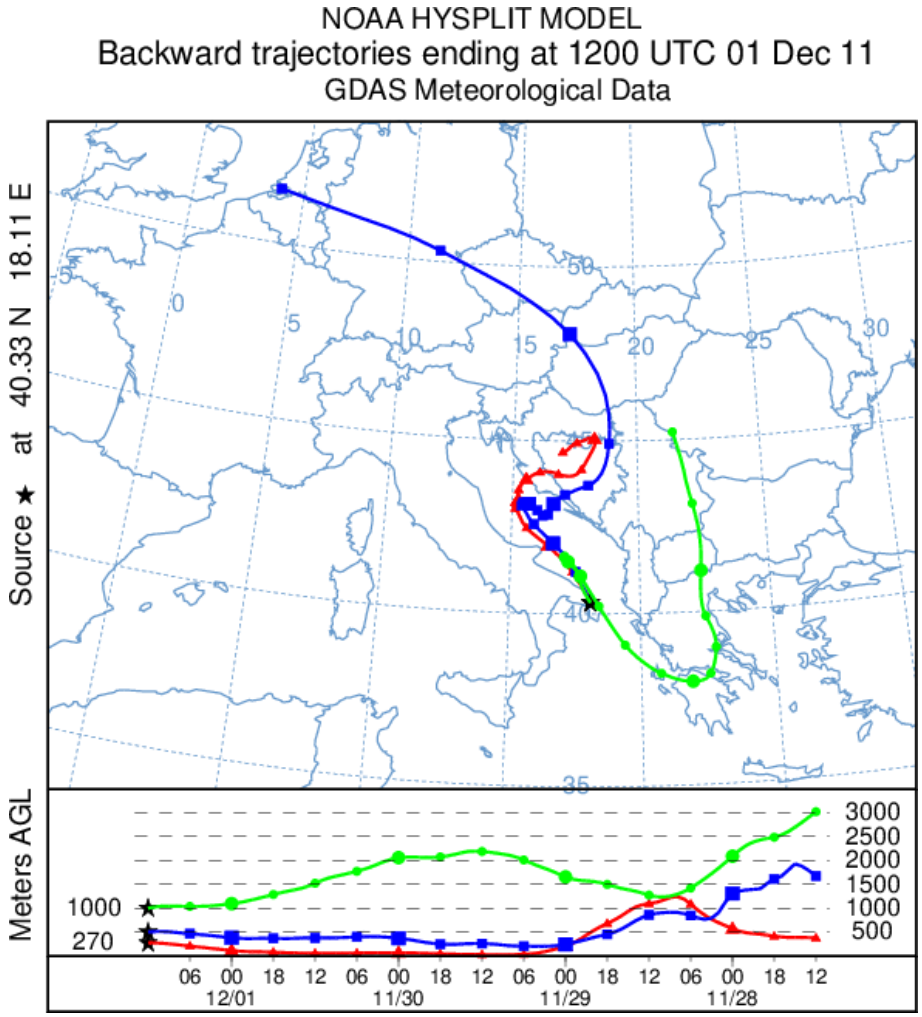


**Figure SM4.** Four-day analytical backtrajectories reaching the study site (40.33°N; 18.11°E) at 270, 500, and 1000 m above ground level (AGL) on 1st December 2011 at 12:00 UTC provided by the HYSPLIT model and corresponding backtrajectory pathways.

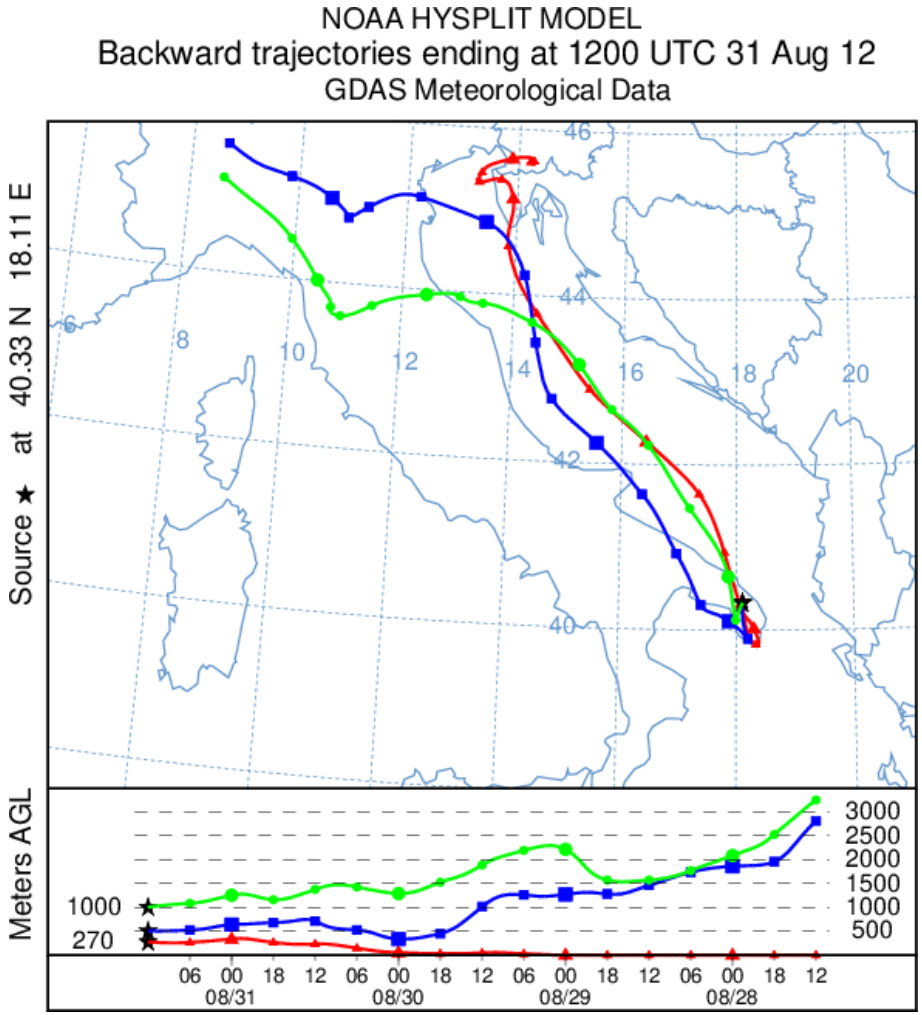


**Figure SM5.** Four-day analytical backtrajectories reaching the study site (40.33°N; 18.11°E) at 270, 500, and 1000 m above ground level (AGL) on 31 August 2012 at 12:00 UTC provided by the HYSPLIT model and corresponding backtrajectory pathways.

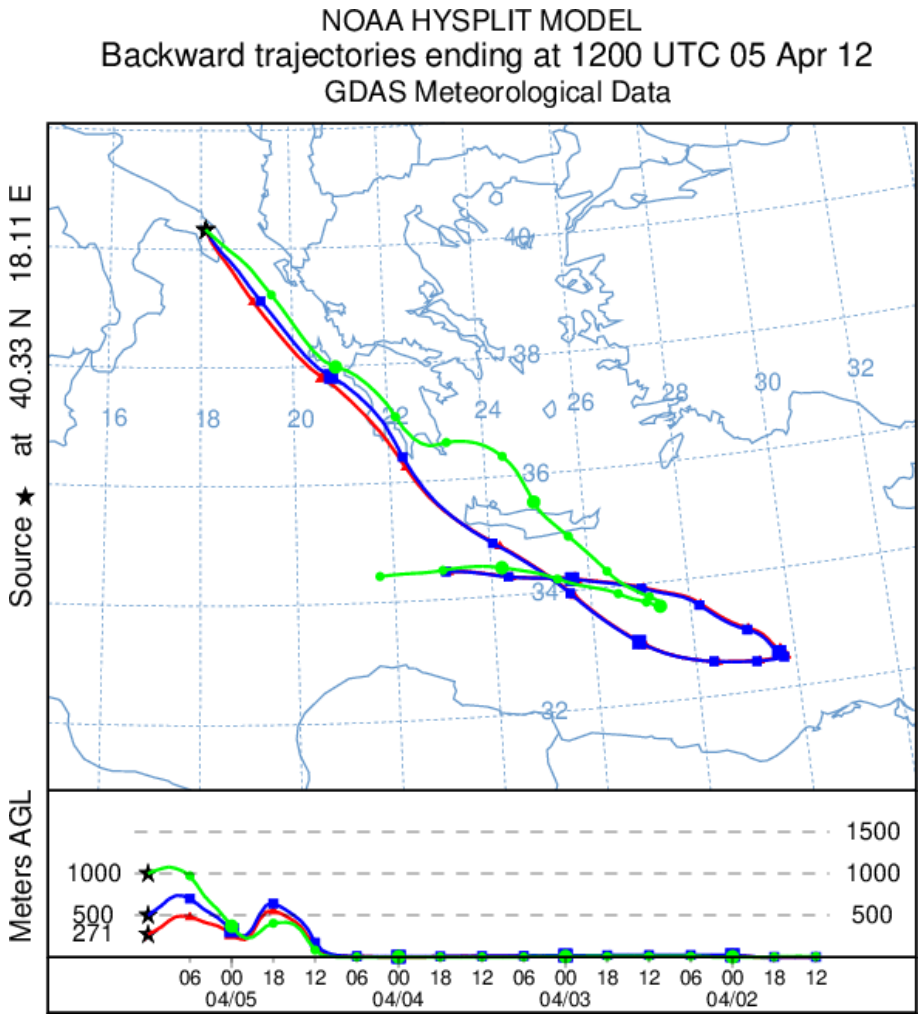


**Figure SM6.** Four-day analytical backtrajectories reaching the study site (40.33°N; 18.11°E) at 270, 500, and 1000 m above ground level (AGL) on 5 April 2012 at 12:00 UTC provided by the HYSPLIT model and corresponding backtrajectory pathways.